

1 |
2 **Visible and short wave infrared reflectance spectroscopy of REE phosphate minerals**

3
4 **DAVID J. TURNER^{1,*}, BENOIT RIVARD², LEE A. GROAT¹**

5
6 ¹Department of Earth, Ocean and Atmospheric Sciences, University of British Columbia, Vancouver,
7 British Columbia V6T 1Z4, Canada

8 ² Department of Earth and Atmospheric Sciences, University of Alberta, Edmonton, Alberta T6G 2E3.
9 Canada

10 *E-mail: dturner@eos.ubc.ca

11 **ABSTRACT**

12 Reflectance spectroscopy in the visible to short-wave infrared regions (500 nm to 2500 nm) was
13 carried out using natural samples of the rare earth element (REE) phosphate minerals monazite,
14 xenotime and britholite. Samples were characterized by scanning electron microscopy and electron
15 microprobe analysis. Absorption band positions were recorded with their probable origins, and spectral
16 variability amongst the samples is discussed. Spectral features of these minerals are driven primarily by
17 $4f-4f$ intraconfigurational electronic transitions of trivalent lanthanides. The distinct REE distributions of
18 monazite, xenotime and britholite drive their bulk spectral patterns, which in turn are sufficiently distinct
19 to enable spectral classification. Spectral variability of some specific REE-related absorptions are
20 interpreted to be driven by differences of the coordination polyhedra for the lanthanide cations between
21 the crystal structures. Spectra of these minerals were also compared against carbonatite-hosted REE
22 bearing fluorapatite. The work presented here strengthens the growing foundation for the interpretation
23 of reflectance spectra of these REE phosphate minerals and enables exploitation of the observed features

24 by the remote sensing community for detection, identification and quantification of REE phosphate
25 minerals. This is especially relevant for hyperspectral imaging spectroscopy with high spatial resolution,
26 where the spectral response of a pixel becomes increasingly dominated by mineralogy.

27 INTRODUCTION

28 The rare earth element (REE) -bearing phosphate minerals monazite, xenotime and britholite are
29 important phases in certain REE deposits and can also be important for geochronology. Monazite and
30 xenotime are found in a wide range of rocks, whereas britholite is more commonly restricted to alkaline
31 igneous complexes, although its distribution is comparatively less well documented. Fluorapatite is a
32 common accessory mineral in many rocks and is also a common host to minor amounts of REE,
33 sometimes reaching substantial concentrations (e.g., up to ~19 wt. % REE₂O₃ at Pajarito Mountain,
34 Roeder et al 1987, Hughes et al. 1991).

35 Monazite, LnPO₄, is composed primarily of the light rare earth elements (LREE) from La
36 through to Gd. Xenotime, also LnPO₄, is composed primarily of the heavy rare earth elements (HREE)
37 from Gd through to Lu and including Y. Despite their similar compositions, monazite and xenotime
38 crystallize in different space groups. Monazite is monoclinic (*P2₁/n*) and xenotime is tetragonal
39 (*I4₁/amd*), in part due to the decreasing ionic radii of the lanthanides from La to Lu and the resulting
40 effect on the coordination polyhedra of the Ln³⁺ and the overall crystal structure. Britholite-(Ce) has the
41 general formula (Ce,Ca)₅(SiO₄)₃(OH) and has been reported with both hexagonal and monoclinic
42 symmetry, however, Oberti et al. (2001) suggest the correct space group is *P6₃*. Fluorapatite,
43 Ca₅(PO₄)₃F, accepts REE³⁺ in place of Ca²⁺ and is generally LREE enriched (e.g., Roeder et al. 1987,
44 Hughes *et al.* 1991). The term *Ln* represents any of the lanthanide elements (La to Lu) while the term
45 REE also includes the geochemically similar element yttrium (Y) and often scandium (Sc).

46 Reflectance spectroscopy, a rapid non-destructive analytical technique requiring little sample
47 preparation, has been used to study the reflectance of these minerals in the visible to short-wave infrared
48 regions. This research builds on the study by Turner et al. (2014) that documented the reflectance spectra
49 of the REE fluorocarbonate minerals bastnaesite, parisite and synchysite. Mineralogical and
50 spectroscopic background of REE-bearing minerals is provided here, followed by a band registry for
51 these phosphate minerals as well as interpretations of spectral absorption features related to the
52 lanthanides. The spectral features of the registry will be the focus of further study in the development of
53 hyperspectral reflectance imaging spectroscopy to carry out REE mineral identification and REE
54 abundance estimates.

55 **GENERAL SPECTROSCOPY OF THE LANTHANIDE ELEMENTS**

56 The outer radius of the $4f$ electron shells ($\sim 0.3 \text{ \AA}$) for the lanthanides is much less than that of
57 their filled $5s$ and $5p$ shells ($\sim 2 \text{ \AA}$, $\sim 1 \text{ \AA}$). It can then be approximated that the local electronic
58 environment of Ln^{3+} cations interacts primarily with those outer shells, leaving the $4f$ electrons relatively
59 sheltered but not completely non-participatory in bonding (e.g., Liu 2005). Electrostatic repulsion of the
60 base ion generates a first-level splitting of spectroscopic states, $2S+1L$ (e.g., 5I). Next, spin-orbit
61 coupling splits these into multiplets, or “J-levels” (e.g., 5I_8), and once placed into a crystal field the J-
62 levels are then split into Stark Sublevels. Crystal field interactions for the Ln cation include variables
63 such as ligand type, coordination number and polyhedron asymmetry which all play roles in the location
64 and intensity of energy levels and the associated absorptions (Görller-Walrand and Binnemans 1998).
65 Each of the resulting sublevels provides the potential for promotion of a relaxed electron into an excited
66 state, giving rise to absorption of electromagnetic radiation (light) at a specific energy level (wavelength
67 or wavenumber).

68 The Dieke Diagram (Dieke et al. 1968) details intraconfigurational $4f-4f$ transitions for ‘free
69 ions’ as deduced through studies of largely mono-lanthanide synthetic compounds. The transitions
70 shown do not include splitting of energy levels due to a crystal field nor the complexities of naturally
71 occurring REE minerals with variable REE distributions and other elemental substitutions.
72 Consequently, this diagram and other band registries (e.g., White 1967) can only act as proxies to help
73 identify origins of absorption features in reflectance spectra of REE minerals. The strength of absorption
74 features due to the lanthanides will primarily be a function of the concentration of the ion as well as the
75 specific absorptivity of that ion’s intraconfigurational transitions within a given crystal structure. The
76 location of lanthanide-related absorption features will be primarily a function of the cation’s specific
77 coordination and asymmetry in the host crystal structure.

78 Synthetic lanthanide and actinide orthophosphates and silicophosphates have also been studied in
79 fairly good detail in research fields such as ceramics, nuclear waste, phosphors and nanotechnology and
80 some studies do include natural samples (e.g., Hayhurst et al. 1981, Bernstein 1982, Becker et al. 1984,
81 Rapaport et al. 1999, Assaaoudi et al. 2001, Cantelar et al. 2001, Carpena et al. 2001, Boatner 2002,
82 Silva et al. 2006, Hernandez and Martin 2007, Zhang and Vance 2008, Ardanova et al. 2010, Savchyn et
83 al. 2012, Lenz et al. 2013, Heuser et al. 2014). These studies generally focus on infrared spectroscopy
84 (400 to 4000 cm^{-1}), Raman spectroscopy and UV-VIS luminescence spectroscopy, however, information
85 can be gathered to help understand and assign absorption bands of natural samples in reflectance spectra.

86 **REVIEW OF REFLECTANCE SPECTROSCOPY STUDIES OF REE-BEARING PHOSPHATE** 87 **MINERALS**

88 The earliest report of reflectance data from REE phosphate minerals is for monazite from 350 to
89 2500 nm (Gerharz 1965), for which no conclusive origin was resolved. In his benchmark mineral
90 spectroscopy paper, Hunt (1977) lists monazite (misspelled as monzonite) in his tabulation of common

91 minerals and respective spectral signatures. However, La^{2+} is listed as the origin of absorptions but La
92 would have a 3+ valence in monazite and would therefore not have spectral features in the VIS-SWIR
93 (e.g., Liu 2005). Amongst many REE-bearing rock sample spectra, Rowan et al. (1986) include a
94 spectrum (400 to 2500 nm) of britholite from Oka (Quebec) and ascribe bands in the VNIR to Nd^{3+} and
95 suggest that a series of bands in the SWIR are related to Sm^{3+} . It is unclear if this is a mineral sample or
96 a britholite-dominant rock sample. Clark (1999) covers several REE oxides in his “Spectroscopy of
97 Rocks and Minerals” review and recognizes that the patterns seen in REE minerals are a combination of
98 several lanthanides, but states that absorptions are independent of mineralogy.

99 The widely used USGS Spectral Library (Clark et al. 2007) contains spectra for fluorapatite,
100 chlorapatite, hydroxylapatite and monazite. The F- and Cl-bearing apatite samples both contain spectral
101 features in the VNIR suggesting minor Nd^{3+} content, whereas the monazite spectrum clearly shows
102 REE³⁺ spectral features. The fluorapatite and monazite spectra are similar to those studied here,
103 however, the data presented here has higher spectral resolution. No xenotime spectra are included in the
104 USGS Spectral Library Version 06.

105 Morin Ka (2012) provides some partial spectra (original data likely collected between 380 and
106 2500 nm) for monazite, xenotime and REE-bearing apatite, but no detailed investigations were carried
107 out. Similarly, Kerr et al. (2011) present spectra from 350 to 2500 nm of monazite, xenotime and REE-
108 bearing apatite but provide no chemical data or interpretation of the spectra. Abstracts by Swayze et al.
109 (2013), Hoefen et al. (2013, 2014) and Huntington and Laukamp (2015) indicate that baseline and
110 applied research is being conducted on REE minerals and deposits, however, no detailed information is
111 available.

112 Thus, there remains an information gap of published material for the interpretation of REE
113 phosphate reflectance spectra, with respect to identifying and explaining spectral features as well as in
114 supporting the discrimination of these phosphate minerals based on their spectral characteristics.

115 **CRYSTAL STRUCTURE REVIEWS**

116 The phosphate classes of REE-bearing minerals show a range of coordination states for REE
117 from eight to 12 with bond lengths as short as 2.25 and as long as ~ 2.8 Å. Cation and anion substitutions
118 in these minerals can be substantial with complex crystal chemical implications, such as in the alunite
119 supergroup. On the other hand, the crystal structures of monazite, xenotime and fluorapatite have been
120 well studied and are well understood.

121 Monazite-(Ce), CePO_4 , and xenotime-(Y), YPO_4 , are very common REE orthophosphate
122 minerals that occur in a wide range of rocks. Despite their similar compositions they have different
123 crystal structures and coordination geometry for the REE site, owing primarily to the size reduction of
124 lanthanides towards Lu. Ni et al. (1995) and Clavier et al. (2011) carried out detailed studies on
125 synthetic REEPO_4 and showed that monazite hosts LREE at a distorted nine-coordinated site whereas
126 xenotime hosts HREE at a higher symmetry eight-coordinated site (Fig. 1). These studies also
127 demonstrated that the REEPO_4 crystals show a systematic decrease in REE-O bond distances when
128 moving from LaPO_4 through to LuPO_4 . Eight of the LREE-O bond lengths for synthetic monazite
129 cluster into three groups between ~ 2.35 and 2.65 Å, with a ninth outlier having a considerably greater
130 length of ~ 2.77 Å (Fig. 2). Mullica et al. (1984) studied the ninefold coordination polyhedron of La in
131 synthetic LaPO_4 and determined that it most closely resembled a distorted pentagonal interpenetrating
132 tetrahedral polyhedron. In xenotime, the bonds are organized into a tighter and more symmetrical
133 structure where four short bonds of ~ 2.25 Å and four medium bonds of ~ 2.35 Å create an HREO_8
134 dodecahedron. The total REO content of natural monazite and xenotime attains 70%.

135 Britholite's more general formula, $(\text{Ce,Ca,Th,La,Nd})_5(\text{SiO}_4,\text{PO}_4)_3(\text{OH,F})$, is chemically and
136 structurally similar to apatite, whereby Si replaces P and REE replaces Ca (Mariano 1989, Oberti et al.
137 2001). Studies of britholite have reported both monoclinic ($P2_1$) and hexagonal ($P6_3$ and $P6_3/m$)
138 symmetry (e.g., Oberti et al. 2001, Pekov et al. 2007). According to refinements by Oberti et al. (2001),
139 the REE can occupy three distinct sites with either nine- (REE1 and REE1a sites, distorted tricapped
140 trigonal prism) or eight- (REE2 site, distorted dodecahedron) coordination (Fig. 1). Bond lengths to the
141 nine-coordinated sites cluster into 2.389, 2.510 and 2.700 Å sets of three each, and for the eight-
142 coordinated site they range from 2.377 to 3.180 Å, averaging ~2.467 Å (Fig. 2). The shortest of these
143 eight bonds is to an OH group. Although the REE1 and REE1a sites are not particularly symmetrical,
144 the REE2 site is highly asymmetrical and is also characterized by two ligand types, hydroxyl and
145 oxygen. Total REO content attains 55%.

146 Fluorapatite, $\text{Ca}_5(\text{PO}_4)_3\text{F}$, has been well studied in a wide range of fields. Its crystal structure is
147 well accepted, and numerous exchange mechanisms have been postulated for the wide variety of
148 substitutions in various rock types. Generally, fluorapatite accepts REE^{3+} in place of Ca^{2+} and Hughes et
149 al (1991) suggest the following dominant coupled substitutions to accommodate charge balancing;
150 $\text{REE}^{3+} + \text{Si}^{4+} = \text{Ca}^{2+} + \text{P}^{5+}$ and $\text{REE}^{3+} + \text{Na}^+ = 2\text{Ca}^{2+}$. Two distinct Ca sites exist (Fig. 1) and the REE
151 have been shown to populate both but have a preference for the Ca(2) site over the Ca(1) site (Fleet and
152 Pan 1995). Using cell refinements of REE-bearing fluorapatite from the Kipawa Complex in Hughes et
153 al. (1991), we see that the Ca(1) site is nine-coordinated with three sets of three oxygen atoms with bond
154 lengths of 2.404, 2.458 and 2.807 Å. The Ca(2) site is seven-coordinated with six Ca-O bonds between
155 2.352 and 2.680 Å, and a bond to F of 2.298 Å (Fig. 2).

156

EXPERIMENTAL METHODS

157 **Samples**

158 Three monazite, four xenotime and two britholite samples from a larger suite were studied in
159 detail with the scanning electron microscope and none showed compositional zoning. One honey-brown
160 monazite crystal ($1 \times 1 \times 1$ cm) from an unknown location was obtained from the Mineralogy/Petrology
161 Museum at the University of Alberta (“537-542 SE Quadrant”) and one similarly sized pinkish-brown
162 monazite fragment from Elk Mountain (Nebraska) was obtained from A. Mariano. The third monazite
163 sample comprising multiple smaller grains is from Serra Verde, Brazil, and was also obtained from A.
164 Mariano. A xenotime sample from Serra Verde that is composed of multiple smaller grains was also
165 obtained. Two euhedral xenotime crystals from Novo Horizonte, Brazil, measured $2.25 \times 0.75 \times 0.75$ cm
166 (sample C) and $2.5 \times 1.4 \times 1$ cm (sample J) and were dark purple in color with patches of transparency.
167 The xenotime sample from Gunter Quarry is a fragment, measures $1.75 \times 2.5 \times 2$ cm, and is opaque and
168 dark brown. Both britholite samples came from the Kipawa deposit in Ontario. One sample was
169 obtained from A. Mariano and comprised several small grains while the second was borrowed from the
170 Canadian Museum of Nature (sample CMNOC F90-8). Hand sample CMNOC F90-8 contains britholite
171 grains measuring on average $\sim 1 \times 1 \times 1$ mm. Reagent-grade lanthanide oxide powders, REE-doped
172 Spectralon wavelength calibration samples and other REE mineral phases were also investigated using
173 EMPA in order to aid in band assignment. Hand samples of dolomitic magnesio-carbonatite from the Fir
174 carbonatite system were used to study spectra from unprobed fluorapatite grains up to 6×3 mm (Chudy
175 2013).

176 **Scanning electron microscopy and electron microprobe analysis**

177 The Philips XL30 scanning electron microscope (SEM) at the University of British Columbia,
178 which is equipped with an energy-dispersion X-ray spectrometer (EDS), was used for preliminary
179 examination of mineral mounts of selected minerals and rock fragments studied by reflectance
180 spectroscopy.

181 Selected samples were then analyzed by electron microprobe at the Saskatchewan Research
182 Council's Advanced Microanalysis Centre using a Cameca SX-100 instrument equipped with five
183 tunable wavelength dispersive spectrometers. Operating conditions were: 40° takeoff angle, beam
184 energy of 15 keV, beam current of 20 nA, beam diameter of 5 µm. The MAN background intensity data
185 was calibrated and continuum absorption corrected. Elements were acquired using analyzing crystals
186 **LLIF** for FeKα, TaLα, PrLα, EuLα, DyLα, TmLα, MnKα, LaLα, NdLα, GdLα, HoLα, YbLα, BaLα,
187 CeLα, SmLα, TbLα, ErLα, LuLα, **PET** for CaKα, KKα, ClKα, TiKα, NbLα, YLα, SrLα, ZrLα, PKα,
188 UMa, ThMa, and **LTAP** for MgKα, FKα, NaKα, SiKα, AlKα. Counting times were 10 seconds for Zr
189 and P and 15 seconds for all other elements, with off-peak count times of 10 seconds. The standards
190 (with elements) were SPI-barite (Ba), SPI-celestite (Sr), SPI-YAG (Y, Al), Smithsonian Cr-augite (Mg,
191 Ca), Smithsonian ilmenite (Fe, Ti), Smithsonian apatite (F, P), Smithsonian microcline (K), Smithsonian
192 zircon (Zr), Harvard albite (Si, Na), Cameca Mn (Mn), SPI2-TiCl (Cl), SPI2-Nb (Nb), SPI2-La (La),
193 SPI2-Ce (Ce), SPI2-Pr (Pr), SPI2-Nd (Nd), SPI2-Sm (Sm), SPI2-Eu (Eu), SPI2-Gd (Gd), SPI2-Tb (Tb),
194 SPI2-Dy (Dy), SPI2-Ho (Ho), SPI2-Er (Er), SPI2-Tm (Tm), SPI2-Yb (Yb), SPI2-Lu (Lu), SPI2-Ta (Ta),
195 SPI2-Th (Th) and SPI2-U (U). Formulae were calculated based on four anions for monazite and
196 xenotime, and 26 anions (O+F+Cl) for britholite. Iron was assumed to be FeO in the one xenotime
197 sample that showed a concentration above detection limit. The amount of OH (as H₂O) was determined

198 by stoichiometry based on full occupation of the “O4” atomic site by two atoms of F, Cl and OH as per
199 Oberti et al. (2001).

200 **Reflectance spectroscopy**

201 Reflectance spectroscopy was primarily carried out using the sisuROCK instrumentation
202 (manufactured by SPECIM Spectral Imaging Ltd.) at the University of Alberta’s CoreSensing Facility,
203 and data were handled using ENVI 4.4, a widely used and commercially available software package.
204 Two imaging spectrometers (“cameras”) acquired reflectance spectra in the visible-near infrared (VNIR,
205 396 nm to 1003 nm over 784 channels for an average spectral resolution of 0.77 nm) and short-wave
206 infrared (SWIR, 928 nm to 2530 nm over 256 channels for an average spectral resolution of 6.26 nm)
207 portions of the electromagnetic spectrum in high spatial resolution mode. Spectralon-based white and
208 striped panels are placed at the head of the imaging table for spectral calibration and camera focusing,
209 and QA/QC procedures carried out automatically by the instrument for each imaging scan. Spatial
210 resolution of the cameras in this mode was approximately 0.079 mm / pixel in the VNIR and 0.241 mm /
211 pixel in the SWIR (Fig. 3). Noise was very prevalent in the shortest wavelength portion of the VNIR
212 camera below ~550 nm and moderate from 550 nm to ~650 nm. In the high spatial resolution mode,
213 averaging spectra of ~16 neighboring pixels resulted in reliable spectra in the noisier ranges that would
214 be useable in spectral libraries. Spectra presented here originate from single crystals, multiple crystals
215 within a single rock sample and from multiple loose single crystals. Spectra documented here are
216 nominally an average of 3215 pixels for the VNIR camera and 1018 pixels for the SWIR camera.
217 Uncommon specular reflections (e.g., as in Fig 3) that saturated detectors were avoided in the selection
218 of pixels. Samples were placed on a matte black surface that translates the samples under the camera and
219 has very low reflectance across the sampled wavelength range. Some samples were propped up with
220 foam blocks to ensure the surfaces of interest faced the spectrometers and were in focus. All samples

221 were thick enough that we could assume that the reflectance spectra are representative of the mineral
222 target.

223 Simple Regions Of Interest (ROI) were used on most samples to select target pixels for
224 averaging. For the loose grains and crystals in hand samples, a priori knowledge of the sample allowed
225 several single-pixel baseline spectra to be isolated. These spectra were then used to apply mixture-tuned
226 matched filtering within the ENVI software package to an entire hyperspectral image, from which a
227 strict qualitative threshold allowed a discrete selection of pixels to be averaged. This process enabled the
228 averaging of tens to hundreds of pixels per sample (Table 1) to produce a representative spectrum as
229 stated above. Reflectance spectra did not have the continuum removed so as to present the data
230 unmodified and to facilitate comparison against data from other publications.

231 **ELECTRON MICROPROBE COMPOSITIONS**

232 Samples described here were selected from a larger set and were characterized by imaging
233 reflectance spectroscopy, scanning electron microscopy and microprobe analysis. Tables 2, 3 and 4
234 document electron microprobe compositions for the REE phosphate minerals in this study and Figure 4
235 shows chondrite-normalized patterns for the samples.

236 Monazite microprobe compositions show similar chemical distributions of the REE for all
237 samples (Table 2), however, the Elk Mountain sample showed slightly higher rare earth elements from
238 Sm onwards. Totals for the Serra Verde and UofA Unk samples are satisfactory, while those for the
239 analyses of the Elk Mountain sample are lower and show high Th and Si contents, indicating
240 substitutions moreso related to huttonite than cheralite (Linthout 2007, Clavier et al. 2011).

241 Xenotime microprobe compositions for the two Novo Horizonte samples show elevated Eu-Gd-
242 Tb-Dy and lesser Yb, Lu and U as compared to the samples from Gunter Quarry and Serra Verde,
243 resulting in two main groups (Table 3). Neodymium and Sm concentrations are roughly equivalent in all

244 four samples, and La, Ce and Pr contents are either very low or below detection. Analytical totals are
245 satisfactory.

246 The two britholite samples originated from different collections but the same ore deposit
247 (Kipawa) and show similar concentrations of REEs (Table 4). Britholite is commonly noted to be at least
248 partially metamict (e.g., Pasero et al. 2010) and in general this is true for samples from Kipawa (e.g.,
249 Noe et al. 1993). The Mariano-001 sample displays a low analytical total while sample CMNOC F90-8
250 is satisfactory for a mineral species commonly reported as metamict. Microprobe compositions show
251 that Ce is the most abundant REE, REE>Ca, Si>P and F>OH,Cl, therefore these samples are
252 fluorbritholite-(Ce).

253 Figure 4 shows the chondrite-normalized EMPA results for selected samples of each mineral to
254 demonstrate relative total REE contents and patterns. Xenotime is strongly enriched in the heavy rare
255 earth elements (HREE) and monazite is enriched in the light rare earth elements (LREE), while
256 britholite contains moderate amounts of all REE.

257 In the case of fluorapatite, published (e.g., Hughes et al. 1991) and unpublished analyses of
258 LREE-enriched fluorapatite from the Fir carbonatite show total rare earth contents near ~5500 ppm. Of
259 the spectrally active REE³⁺, the measured Pr content is ~300 ppm, Nd ~1200 ppm and Sm ~200 ppm.

260 **SPECTRA AND SPECTRAL VARIABILITY OF REE-PHOSPHATE MINERALS**

261 Each of the three REE-phosphate minerals exhibits its own characteristic distribution of rare
262 earth elements and therefore spectral patterns derived from 4*f*-4*f* intraconfigurational electronic
263 transitions. As seen from microprobe compositions, xenotime is populated by the heavy rare earths (Gd
264 to Lu), monazite by the light rare earths (La to Sm) and britholite accommodates both lights and heavies
265 yet has lower overall REE contents (Fig. 4 and Tables 2 to 4). Fluorapatite is generally enriched in
266 LREE (e.g., Hughes et al. 1991).

267 Figures 5, 6, 7 and 8 document the spectra from samples of each mineral and show the location
268 of prominent absorptions and absorption clusters listed in Tables 5, 6 and 7. These “Band Index Tables”
269 document prominent absorption features for the REE phosphate minerals and include probable origins of
270 the features, as chosen through comparison with reflectance spectra from unpublished reagent-grade
271 lanthanide oxide spectra, REE-doped calibration standard spectra, and other REE-bearing mineral
272 spectra for which compositional data exists, as well as REE spectroscopy literature. Clusters are
273 numbered and denoted in the Tables by horizontal line breaks and important absorptions are bolded. As a
274 set of summary figures, clusters and main absorption features are shown on “Index Figures” 9 (VNIR
275 range) and 10 (SWIR range) for representative spectra of monazite, britholite and xenotime.

276 The UofA Unk monazite, CMNOC Kipawa britholite, Gunter Quarry and Novo Horizonte J
277 xenotime samples were used in the Index Tables because of their superior microprobe results. Band
278 indices for all samples can be found in Turner (2015).

279

280 **Monazite reflectance spectra**

281 The Serra Verde and UofA Unk monazite samples have fairly similar elemental distributions,
282 however, the sample from Elk Mountain shows higher medium REE values and considerably higher Th
283 and Si and lower P than the other two samples.

284 The VNIR spectral range is divided into seven main clusters of absorptions (Fig. 5, Table 5). The
285 most notable differences in the VNIR spectra of the three monazite samples are the strengths of the 652
286 and 671 nm absorptions of Cluster 2, which are strongest in the sample from Serra Verde. The
287 absorption band at 978 nm (Cluster 7) also shows some variability in strength, being most pronounced in
288 the spectrum of the Elk Mountain sample and weakest in the spectrum of the UofA Unk sample.

289 The SWIR spectral range is divided into five main clusters of absorptions starting after Clusters
290 6 and 7, which are better resolved in the VNIR range (Fig. 5, Table 6). Spectra for the monazite samples
291 in the SWIR range are very consistent. Subtle differences include a shift in the ~1960 nm feature and the
292 relative intensities of absorption bands at ~2424 and ~2499 nm.

293 **Xenotime reflectance spectra**

294 Chemical differences separate the two xenotime samples from Novo Horizonte (higher Eu, Gd,
295 Tb, Dy) from those from Serra Verde and Gunter Quarry (higher Yb, Lu, U). Bulk patterns are consistent
296 across all xenotime samples, however, the notable chemical distributions give rise to spectral differences
297 in both the VNIR and SWIR.

298 The VNIR spectral range is divided into six main clusters of absorptions (Fig. 6, Table 7).
299 Differences in the VNIR spectra across the two groups of xenotime samples are typically slight, such as
300 the presence or absence of a shoulder feature or the relative depth of a specific absorption. The Novo
301 Horizonte samples show stronger absorptions at 643, 690, 760, 827, 932 and 961 nm while the Gunter
302 Quarry and Serra Verde samples show stronger absorptions at 669, 678 and 803 nm. These two groups
303 hold true for other unpublished xenotime VNIR spectra that show similar spectral patterns but that do
304 not have supporting microprobe compositions.

305 The SWIR spectral range is divided into eight clusters beyond 978 nm, where Cluster 6 is better
306 described in the VNIR range (Fig. 6, Table 7). Differences in the SWIR spectra across the two groups of
307 xenotime samples are most prominent in clusters 7, 12 and 14. Cluster 7 differences are driven by
308 relative contents of Dy and U in the two groups. The high U content of the Gunter Quarry and Serra
309 Verde samples results in the prominent absorption being at 1143 nm, while the high Dy content of the
310 Novo Horizonte C and J samples results in the prominent absorption being at 1099 nm. For Cluster 12,
311 the prominent absorption at 1880 nm is consistent with the relative proportions of Tb in the xenotime

312 samples. Cluster 14 comprises absorptions from 2150 nm to the end of the detection range of the
313 spectrometer at 2530 nm, and is discussed in more detail later.

314 **Britholite reflectance spectra**

315 The two britholite samples have very similar REE distributions, however, their bulk
316 compositions differ. The CMNOC F90-8 sample shows totals closer to 100% and better cation
317 populations after formula normalization by anion content. This sample shows lower La and Ce contents,
318 equivalent Pr through Lu and higher Y, as well as higher P, Si, Th, Ca and OH contents.

319 The VNIR spectral range is divided into six main clusters of absorptions (Fig. 7, Table 5). The
320 only significant difference between the two spectra is how Cluster 1 is resolved into two features in
321 sample “001-Mariano”, which generally shows stronger absorptions elsewhere.

322 The SWIR spectral range is divided into six clusters beyond the 978 nm absorption, which is
323 ascribed to Cluster 6 in the VNIR range (Fig. 7, Table 6). Absorptions in Clusters 11 and 12 show slight
324 variations.

325 **Fluorapatite reflectance spectrum**

326 The fluorapatite spectrum was derived from one crystal with distinct grain boundaries in a cut
327 rock slab with an abundance of fluorescent fluorapatite, all of which show spectra with equivalent
328 absorptions in the VNIR and SWIR. Although the absorptions were weaker in fluorapatite, general
329 cluster locations were consistent with the LREE-enriched monazite and britholite sample spectra (Tables
330 5 and 6).

331 Generally, the reflectance spectrum of pure fluorapatite in the SWIR range is featureless (e.g., as
332 in the USGS Spectral Library, Clark et al. 2007), however, the SWIR reflectance spectrum for this
333 sample is dominated by absorption bands consistent with ferroan dolomite (e.g., minima at 2318 and

334 2499 nm with continuum removed; Gaffey 1986). Subtle but narrow absorptions in this fluorapatite
335 spectrum occur within the broader ~1200 nm Fe-related absorption, and are likely associated with
336 REE³⁺. The ferroan dolomite signals are likely due to microscopic inclusions within the fluorapatite
337 crystal, however, carbonate has also been shown to exist as a minor component in some hydroxylapatite
338 and fluorapatite (e.g., Fleet and Liu, 2008).

339 **DISCUSSION OF SPECTRA AND SPECTRAL VARIATIONS**

340 **REE compositional controls on reflectance spectra**

341 The typical distribution of rare earth elements in monazite (LREE), xenotime (HREE), britholite
342 (LREE and HREE) and fluorapatite (LREE) directly affects their spectral signatures. For naturally
343 occurring minerals the most important LREE that are spectrally active in the VNIR-SWIR range are
344 Pr³⁺, Nd³⁺ and Sm³⁺. Similarly, the most important spectrally active HREE for minerals are Dy³⁺, Er³⁺
345 and Yb³⁺ but Tb³⁺, Ho³⁺ and Tm³⁺ still need to be considered. Therefore, typical REE distribution for a
346 given mineral means that it will also display a typical distribution of *spectrally active* REE³⁺. This
347 allows for quick recognition of a mineral's bulk REE distribution but more subtle spectral features then
348 need to be considered when addressing mineral identification.

349 Accordingly, the most notable differences between the mineral samples are driven by the relative
350 distributions of light versus heavy rare earth elements. Monazite is LREE-enriched and thus its spectral
351 signature is driven primarily by Nd³⁺ with lesser influence by Pr³⁺ and Sm³⁺, while HREE-enriched
352 xenotime has spectral features driven primarily by Yb³⁺, Er³⁺ and Dy³⁺. The britholite spectrum is
353 dominated by Nd³⁺ with lesser influence by Pr³⁺ and Sm³⁺ but signals of Dy³⁺, Er³⁺ and Yb³⁺ are
354 observed. Consequently, britholite spectra more closely resemble spectra of monazite than xenotime and
355 a good understanding of the spectral characteristics of britholite can be derived by 'modifying' monazite

356 spectra with minor input from Dy⁺³, Er⁺³ and Yb⁺³. The fluorapatite spectrum shows absorptions related
357 to Nd³⁺ in the VNIR, and possible weak absorptions related to Sm³⁺ and Pr³⁺ in the SWIR.

358 Spectral differences between xenotime samples are minor, usually only a variation in the strength
359 of a feature. Unlike LREE minerals dominated by Pr³⁺, Nd³⁺ and Sm³⁺ spectral features, in minerals with
360 abundant HREE it is harder to definitively assign individual features to individual lanthanide elements
361 because many of the multiplet levels from Sm³⁺, Tb³⁺, Dy³⁺, Ho³⁺, Er³⁺, Tm³⁺ and Yb³⁺ overlap. Some of
362 the multiplet levels can produce many absorptions of varying strength as deduced through mono-
363 lanthanide doping studies of various compounds (e.g., Ho³⁺:YGG by Gruber et al. 2009).

364 **Comparison of absorption patterns for monazite, xenotime, britholite and fluorapatite**

365 Figures 9 and 10 show representative spectra for xenotime, britholite and monazite in the VNIR
366 and SWIR ranges with absorption clusters and distinct absorptions labeled. Samples “UofA Unk” for
367 monazite, “Gunter Quarry” for xenotime and “Kipawa CMNOC F90-8” for britholite are used as the
368 base lines for describing intermineral variations. The monazite sample shows the nearest chemical
369 composition to ideal monazite, the xenotime sample represents one of the two spectral-chemical
370 populations and the britholite sample shows the highest total from microprobe data and better atomic
371 site assignments.

372 When comparing spectra of monazite to britholite, which have similar LREE concentration
373 patterns, trends of shifting band minima and band broadening emerge (Figs. 9 and 10). Many absorption
374 minima related to Nd³⁺ undergo systematic shifts to longer wavelengths in britholite as compared to
375 monazite. Shifted bands (from monazite to britholite) in the VNIR include 679 nm to 685 nm, 745 nm to
376 747 nm, 800 nm to 805 nm, 863 nm to 867 nm and 871 nm to 879 nm.

377 The absorptions for britholite are generally broader and show less structure, most likely
378 attributable to multiple REE sites and therefore multiple overlapping bands in close proximity. For

379 example, the fine structure of the Nd³⁺-related 745 nm absorption of monazite is lost in britholite except
380 for a weak shoulder at 743 nm. The many local minima from 871 to ~900 nm in monazite are also lost in
381 britholite, likely due to REE site multiplicity and resulting fine band shifts and overlap.

382 Turner et al. (2014) described the reflectance spectra of REE fluorocarbonate minerals and noted
383 that the Sm³⁺-related features at 1093 nm and 1251 nm are quite sharp. In monazite, these two features
384 are each consistently split into two discrete absorptions at 1074 and 1105 nm and at 1232 and 1257 nm
385 (Fig. 10). The barycenter of the absorptions in monazite remains close to that of the REE
386 fluorocarbonate minerals. In britholite, concentrations of Sm are lower, however, the splitting appears
387 greater near 1251 nm with a strong band minima at 1225 and a shoulder at 1257 nm (Fig. 10). Near 1093
388 nm, the absorptions in britholite broaden with minima at 1074 nm and a weak shoulder at 1105 nm. The
389 weaker Sm³⁺-related absorption at 953 nm in bastnaesite is similarly split to 941 nm and 957 nm in
390 monazite (Fig. 9). In britholite, however, this absorption is not seen due to again lower Sm contents.

391 Fluorapatite absorptions can all be attributed to Nd³⁺ in the VNIR and occur in the same regions
392 as for monazite and britholite, however, the absorptions near 870 nm are much more subdued, possibly
393 due to the influence of an Fe²⁺ band from ferroan dolomite (Gaffey 1986), and the Cluster 2 Nd³⁺
394 absorptions seen in the monazite spectra are not resolvable in the fluorapatite spectrum. The most
395 notable aspect of the fluorapatite spectrum is the pronounced pair of minima at 576 and 585 nm, which
396 is not seen as a resolved pair in either monazite or britholite (Fig. 11).

397 **The Yb-Er related absorption near 978 nm**

398 Britholite and xenotime show an absorption feature at 978 nm that is related to both Yb³⁺ ($^2F_{7/2}$
399 \rightarrow $^2F_{5/2}$) and Er³⁺ ($^4I_{5/2} \rightarrow$ $^4I_{11/2}$). This particular Yb³⁺ transition is known to be hypersensitive to its
400 immediate coordination polyhedron and also absorbs more strongly than Er³⁺ at this wavelength (e.g.,
401 Zou and Toratani 1995, Strohhofer and Polman 2003). In britholite, the strength of the 978 nm

402 absorption is equal to or stronger than in xenotime (Fig. 12), despite the concentrations of Er and Yb
403 being *lower* by a factor of ~4 in britholite (Tables 3 and 4, and Fig. 4). Thus, the absorption coefficient
404 for this particular Yb³⁺ hypersensitive transition is much stronger in britholite than in xenotime. This is
405 most probably due to the REE site in britholite being more asymmetric than in xenotime (Figs. 1 and 2),
406 as well as being better suited to host REE³⁺ cations with larger ionic radii, such as Ce³⁺, rather than the
407 smaller Yb³⁺.

408 **Spectral effects of the actinides**

409 Electronic absorption bands for the 5*f* energy levels of U^{4+,5+} are reported to be strongest near
410 ~2069, ~1500, ~1330 and ~1111 nm in the SWIR and ~666 nm in the VNIR (e.g., Binnemans et al.
411 1999, Zhang et al. 2002, 2003), however, all of these bands are also within the ranges of various other
412 REE³⁺ absorptions. Xenotime from Serra Verde contains the most uranium of all the samples studied
413 with 1.59 wt.% UO₂ while those from Novo Horizonte have ~0.05 wt.% UO₂. Probable resolvable
414 absorptions related to U in xenotime were noted at 653, 1118, 1143 and 1503 nm, as interpreted through
415 comparison with zircon spectra (e.g., Zhang et al. 2002, 2003, and Turner 2015) and considering EMPA
416 data.

417 **Hydroxyl and water bands of the REE phosphate minerals**

418 Xenotime and monazite can accommodate minor amounts of OH in their crystal structures, trap
419 fluid inclusions during growth, and become metamict through radiation damage related to decay of U
420 and Th which can then lead to hydration (e.g., Talla et al. 2011). The xenotime samples studied here
421 contain low amounts of charge-balancing anions and are not considered to be appreciably metamict.
422 Monazite shows generally higher calculated OH content and also considerably more Th. Britholite
423 normally accommodates OH and some samples from Kipawa studied by others have been shown to be

424 partially metamict (e.g., Noe et al. 1993). Consequently, the monazite and britholite samples show
425 absorption bands at 1377 nm that are related to OH and near ~1950 nm that are related to water and
426 REE. Xenotime spectra show bands from 1408 to 1415 nm that are related to an OH overtone, which is
427 consistent with Talla et al. (2011) who identified stretching vibrations near 3500 cm^{-1} in xenotime. The
428 bands near 1936 nm are more likely tied to the Ho^{3+} and Tb^{3+} content but may also be influenced by
429 water.

430 **Absorptions from 2150 nm to 2530 nm**

431 Spectra of the REE phosphate minerals display a number of overlapping absorptions expressed
432 as minima and shoulders between 2150 nm ($\sim 4650\text{ cm}^{-1}$) and 2530 nm ($\sim 3953\text{ cm}^{-1}$). As a general
433 statement, each mineral shows moderate consistency between the samples, but significant differences
434 are observed in the two classes of xenotime samples (Figs. 5, 6 and 7). The exact origin of these
435 absorption bands remains unclear.

436 In their study of hydrated and hydroxylated phosphate minerals [e.g., childrenite –
437 $\text{FeAlPO}_4(\text{OH})_2 \cdot \text{H}_2\text{O}$], Lane et al. (2011) show reflectance spectra with sharp absorptions in the 2100 to
438 2500 nm range, which they attribute to overtones and combinations of OH and PO_4 vibrations. In a
439 similarly themed study of hydrated hydroxylated phosphate minerals [e.g., wardite –
440 $\text{NaAl}_3(\text{PO}_4)_2(\text{OH})_4 \cdot 2\text{H}_2\text{O}$], Frost and Erickson (2005) ascribed bands from ~ 4600 to 4000 cm^{-1} (2174 to
441 2500 nm) to combinations of OH stretching and OH deformational vibrations. Assaaoudi et al. (2001)
442 and Onac et al. (2005) reported that amongst different hydrated orthophosphates (e.g., churchite,
443 $\text{YPO}_4 \cdot 2\text{H}_2\text{O}$), small band shifts of the fundamental vibrations for P-O, O-H and H-O-H are potentially
444 related to variable REE content. Talla et al. (2011) studied OH defects in xenotime and identified an OH-
445 stretching mode near 3500 cm^{-1} ($\sim 2850\text{ nm}$). Combining that stretching mode with a fundamental PO_4
446 vibration near 1000 cm^{-1} (e.g., Farmer 1974) results in a potential combination band near 4500 cm^{-1}

447 (2222 nm). Small absorptions near 4500 cm^{-1} can be seen in one IR spectral plot of xenotime from
448 Talla et al. (2011), but are not discussed in the paper. Pekov et al. (2007) recorded overlapping Si-O and
449 P-O bands for metamict fluorcalciobriholite at 930 and 1070 cm^{-1} (10753 and 9346 nm), respectively,
450 and Oberti et al. (2001) recorded a broad OH-stretching band at 3437 cm^{-1} (2910 nm) in fluorbriholite
451 but no spectrum was provided. Thus, theoretical calculations of combination bands for the REE
452 phosphate minerals support the notion of their influence in this region between 2150 and 2530 nm,
453 however, neither xenotime nor monazite have structural OH or H_2O in any great amounts and
454 reflectance spectra consistently show more than one resolved band.

455 Trivalent lanthanide elements with electronic energy levels in the ~2150 to 2500 nm range (4650
456 cm^{-1} to 3953 cm^{-1}) include Pr^{3+} (~2310 nm, $^3\text{H}_6$) and Tb^{3+} (~2200 nm, $^7\text{F}_3$) with potential influence from
457 Nd^{3+} (~2500 nm, $^4\text{I}_{13/2}$) and Eu^{3+} (~2100 nm, $^7\text{F}_6$) when placed in a crystal field, according to energy
458 levels recorded by Dieke et al. (1968) and Carnall et al. (1989). Reflectance spectra for REE_2O_3 reagents
459 and reflectance and transmission data available from the literature in this range suggest that REE-related
460 absorptions could be responsible for the patterns seen in the REE phosphate minerals. In particular, Talla
461 et al. (2011) synthesized REE-doped xenotime with Pr, Nd, Sm, Dy, Ho and Er and collected polarized
462 IR absorption spectra from 7000 to 2500 cm^{-1} (1429 – 4000 nm). Of these synthetic xenotime crystals,
463 the Nd-doped sample exhibits two (possibly three) bands at approximately 2400 and 2475 nm (the third
464 near 2500 nm) and the Pr-doped sample exhibits only one band near 2375 nm. Unfortunately neither
465 Eu_2O_3 nor Tb_2O_3 were included in their EMPA results for their natural samples and they did not
466 synthesize Eu- or Tb-doped xenotime. It is unlikely that Eu would play a significant role due to
467 relatively low contents, however, Tb_2O_3 concentrations in xenotime can be appreciable. Focusing just on
468 xenotime, the two samples from Novo Horizonte have the highest Tb_2O_3 contents and show the
469 strongest absorptions near 2262 nm and 2312 nm, suggesting that at least these two bands are linked to

470 Tb³⁺. Looking back at the one natural sample shown by Talla et al. (2011) in this range (their Fig. 7),
471 two more small absorption features can be seen near 2247 and 2325 nm. Thus, with the spectra from
472 Talla et al. (2011) but without spectra from Tb-doped xenotime it is still difficult to conclusively tie
473 intramineral chemical variations to spectral variations.

474 A spectrum from reagent grade La powder [qualitatively determined as La(OH)₃ >> La₂O₂(CO₃)
475 through powder X-ray diffraction, see Turner 2015] shows absorption bands in the 2300 to 2500 nm
476 range (in addition to water related absorptions at ~1420 nm and ~1950) but La³⁺ should not show *4f-4f*
477 electronic transitions as it has no electrons in the *f* orbital. Conversely, reagent grade Gd₂O₃, Y₂O₃ and
478 Yb₂O₃ powders show minor absorptions near 1420 and 1950 nm but no distinct absorptions between
479 2300 and 2500 nm. Consequently, it is apparent that at least *some* REE reagents are generating
480 absorptions related to REE-OH bonding (with possible CO₃ absorptions), thus making interpretations of
481 other REE-related absorptions in this region difficult.

482 If absorptions in this region were solely attributable to PO₄ / OH vibrational combinations we
483 would expect more coherency between the PO₄ minerals, less variability in the xenotime spectra, and
484 weaker absorptions where OH is minimal (i.e., xenotime and monazite vs. britholite). If these
485 absorptions were solely the result of REE³⁺ electronic transitions we would expect greater support from
486 the existing REE-spectroscopy literature and not observe absorptions in La₂O₃. If they were solely the
487 result of REE-OH vibrational bands we would expect to see more systematic variations within and
488 across the phosphate groups. It is therefore most likely that each of these factors plays a role in
489 absorptions from 2150 to 2530 nm, but without further investigations using additional techniques it is
490 difficult to determine the exact origins of these absorption bands across monazite, britholite and
491 xenotime.

492

IMPLICATIONS

493 This work is the first published systematic study of the REE-phosphate minerals monazite,
494 xenotime and britholite using reflectance spectroscopy in the VNIR-SWIR range. Spectra coupled with
495 microprobe compositions indicate that spectra of monazite and britholite are dominated by Nd^{3+} , Pr^{3+} ,
496 and Sm^{3+} -related absorption bands. The multiple atomic sites with mixed coordination for Ln^{3+} in
497 britholite allows for easy incorporation of Tb, Dy, Ho, Er, Tm and Yb. The mixed coordination of cation
498 sites REE1/REE1a (nine-coordinated) and REE2 (eight-coordinated) results in multiple sets of crystal
499 field splitting for the Ln^{3+} , thus potentially broadening each absorption band related to electronic
500 transitions. The xenotime spectrum is dominated by the distribution of HREE, namely Tb^{3+} , Dy^{3+} , Ho^{3+} ,
501 Er^{3+} , Tm^{3+} and Yb^{3+} . Many of the energy levels for these elements overlap, making definitive
502 assignments of probable origin difficult; however, absorption clusters are consistent across samples. The
503 reflectance spectrum of LREE-bearing fluorapatite was shown to have strong similarities to monazite
504 and britholite spectra in the VNIR range, however, the Nd^{3+} -related absorptions near 576 and 585 nm
505 show distinct differences in band positions.

506 The sensitive nature of the Yb^{3+} and Er^{3+} transitions near 978 nm are well illustrated between
507 xenotime and britholite. Despite xenotime having significantly higher concentrations of Yb and Er,
508 britholite exhibits an equally strong absorption band at this wavelength because of the greater
509 asymmetry of the coordination polyhedra compared to xenotime.

510 These data provide the diverse geological remote sensing community with a benchmark to which
511 comparison can be made regarding spectra with Ln^{3+} -related electronic absorptions. Diagnostic
512 variations between the REE phosphate minerals can also be exploited in a number of circumstances,
513 such as remote predictive mapping, petrology of thin sections and rocks, identifying potential mineral
514 grains for geochronology, drill core and chip logging, mine wall imaging or ore sorting.

515 Future work should include a systematic study of mono-lanthanide doped phosphate crystals, as
516 well as continuing to add other REE phosphate minerals with variable REE content. Spectral range
517 should be expanded to include regions of fundamental vibrations in the same mineral suites (i.e., 400 to
518 4000 cm^{-1}). This will enhance the growing database of REE mineral reflectance spectra and help clarify
519 ambiguity for assigning absorptions to specific lanthanides across the entire VNIR-SWIR range, but
520 especially from 2150 to 2530 nm.

521 ACKNOWLEDGEMENTS

522 Tony Mariano and Michel Picard (Canadian Museum of Nature) are thanked for their help with
523 acquiring samples, and Jilu Feng and Steve Creighton for their help with data collection. Financial
524 support is acknowledged from the Natural Sciences and Engineering Research Council of Canada. Dr.
525 Chudy is thanked for his help and insight with the fluorapatite-bearing Fir carbonatite sample.
526 Reviewers X, Y and Z provided constructive reviews that improved the quality and clarity of this
527 manuscript.

528 REFERENCES

- 529 Ardanova, L. I., Get'man, E. I., Loboda, S. N., Prisedsky, V. V., Tkachenko, T. V., Marchenko, V. I., ... &
530 Lyashenko, A. S. (2010). Isomorphous substitutions of rare earth elements for calcium in synthetic
531 hydroxyapatites. *Inorganic chemistry* 49, 10687-10693.
- 532 Assaoudi, H., Ennaciri, A., & Rulmont, A. (2001). Vibrational spectra of hydrated rare earth
533 orthophosphates. *Vibrational Spectroscopy* 25, 81-90.
- 534 Becker, P. C., Hayhurst, T., Shalimoff, G., Conway, J. G., Edelstein, N., Boatner, L. A., & Abraham, M. M.
535 (1984). Crystal field analysis of Tm^{3+} and Yb^{3+} in YPO_4 and LuPO_4 . *The Journal of chemical physics* 81,
536 2872-2878.

- 537 Bernstein, L. R. (1982). Monazite from North Carolina having the alexandrite effect. *American Mineralogist* 67,
538 356-359.
- 539 Binnemans, K., Couwenberg, I., De Leebeeck, H., Görrler-Walrand, C., & Adam, J. L. (1999). Spectroscopic
540 properties of tetravalent uranium in glasses. *Journal of Alloys and Compounds* 285, 105-111.
- 541 Boatner, L. A. (2002). Synthesis, structure, and properties of monazite, pretulite, and xenotime. *Reviews in*
542 *mineralogy and geochemistry* 48, 87-121.
- 543 Cantelar, E., Lifante, G., Calderón, T., Meléndrez, R., Millán, A., Alvarez, M. A., & Barboza-Flores, M. (2001).
544 Optical characterisation of rare earths in natural fluorapatite. *Journal of Alloys and Compounds*, 323, 851-
545 854.
- 546 Carnall, W. T., Goodman, G. L., Rajnak, K., & Rana, R. S. (1989). A systematic analysis of the spectra of the
547 lanthanides doped into single crystal LaF₃. *The Journal of Chemical Physics* 90, 3443-3457.
- 548 Carpéna, J., Boyer, L., Fialin, M., Kiénast, J. R., & Lacout, J. L. (2001). Ca²⁺, PO₄³⁻ ⇌ Ln³⁺, SiO₄⁴⁻ coupled
549 substitution in the apatitic structure: stability of the mono-silicated fluor-britholite. *Comptes Rendus de*
550 *l'Académie des Sciences-Series IIA-Earth and Planetary Science* 333, 373-379.
- 551 Chudy, T.C. (2013). The petrogenesis of the Ta-bearing Fir carbonatite system, east-central British Columbia,
552 Canada. Unpublished PhD Thesis, University of British Columbia, Canada. 585 pages.
- 553 Clark, R. N. (1999). Chapter 1: Spectroscopy of Rocks and Minerals, and Principles of Spectroscopy, In: *Manual*
554 *of Remote Sensing, Volume 3, Remote Sensing for the Earth Sciences* 3-58.
- 555 Clark, R. N., Swayze, G. A., Wise, R. A., Livo, K. E., Hoefen, T. M., Kokaly, R. F., & Sutley, S. J. (2007). USGS
556 digital spectral library splib06a, U.S. Geol. Surv. Digital Data Ser. 231p.
- 557 Clavier, N., Podor, R., & Dacheux, N. (2011). Crystal chemistry of the monazite structure, *Journal of the*
558 *European Ceramic Society* 31, 941-976.

- 559 Dieke, G. H., Crosswhite, H., & Crosswhite H.M., (1968). Spectra and energy levels of the rare earth ions in
560 crystals. New York: Wiley Interscience, 193 p.
- 561 Farmer, V. C. (1974). *Infrared spectra of minerals*. Mineralogical society. 539 p.
- 562 Fleet, M.E., & Liu, X. (2008). Accommodation of the carbonate ion in fluorapatite synthesized at high pressure.
563 *American Mineralogist*, 93, 1460-1469.
- 564 Frost, R. L., & Erickson, K. L. (2005). Near-infrared spectroscopic study of selected hydrated hydroxylated
565 phosphates. *Spectrochimica Acta Part A: Molecular and Biomolecular Spectroscopy* 61, 45-50.
- 566 Gaffey, S. J. (1986). Spectral reflectance of carbonate minerals in the visible and near infrared (0.35-2.55
567 microns); calcite, aragonite, and dolomite. *American Mineralogist*, 71, 151-162.
- 568 Gerharz, R. (1965). Absorption structures in the visible reflection spectrum of minerals. *Economic Geology* 60,
569 1721-1725.
- 570 Görrler-Walrand, C., & Binnemans, K. (1998). Spectral intensities of *f-f* transitions, *In: Handbook on the Physics*
571 *and Chemistry of Rare Earths*, Vol. 25, Chapter 167, editors: K.A. Gschneidner and L. Eyring (North-
572 Holland Publishers, Amsterdam, 1998), 101-264.
- 573 Gruber, J. B., Burdick, G. W., Valiev, U. V., Nash, K. L., Rakhimov, S. A., & Sardar, D. K. (2009). Energy levels
574 and symmetry assignments for Stark components of Ho³⁺ (4f¹⁰) in yttrium gallium garnet
575 (Y₃Ga₅O₁₂). *Journal of Applied Physics* 106, 113110.
- 576 Hayhurst, T., Shalimoff, G., Edelstein, N., Boatner, L. A., & Abraham, M. M. (1981). Optical spectra and
577 Zeeman effect for Er³⁺ in LuPO₄ and HfSiO₄. *The Journal of Chemical Physics* 74, 5449-5452.
- 578 Hernández, T., & Martin, P. (2007). Microstructural and optical features of a Eu-monazite. *Journal of the*
579 *European Ceramic Society* 27, 109-114.

- 580 Heuser, J., Bukaemskiy, A. A., Neumeier, S., Neumann, A., & Bosbach, D. (2014). Raman and infrared
581 spectroscopy of monazite-type ceramics used for nuclear waste conditioning. *Progress in Nuclear*
582 *Energy* 72, 149-155.
- 583 Hoefen, T. M., Swayze, G., Giles, S.A., Van Gosen, B.S., Emsbo, P., & Karst, A. (2013). Spectroscopic
584 investigations of REE hosted heavy mineral sands and phosphates. In *Geological Society of America*
585 *Abstracts with Programs* 45, 278.
- 586 Hoefen, T. M., Livo, K. E., Giles, S. A., Lowers, H. A., Swayze, G. A., Taylor, C. D., Verplanck, P.L., Emsbo, P.,
587 Koenig, A., & Mccafferty, A. E. (2014). Characterization of REE-Bearing Minerals and Synthetic
588 Materials Using High Resolution Ultraviolet to Near-Infrared Reflectance Spectroscopy. In *AGU Fall*
589 *Meeting Abstracts* 1, 4299.
- 590 Hughes, J. M., Cameron, M., & Mariano, A. N. (1991). Rare-earth-element ordering and structural variations in
591 natural rare-earth-bearing apatites. *American Mineralogist* 76, 1165-1173.
- 592 Hunt, G.R. (1977). Spectral signatures of particulate minerals, in the visible and near-infrared, *Geophysics* 42,
593 501-513.
- 594 Huntington, J., & Laukamp, C. (2015): Drill core reflectance spectroscopy applied to the carbonatite hosted REE
595 deposit at Cummins Range (Australia). *SGA 2015, August 24-27, Nancy, France*. 1017–1019.
- 596 Kerr, A., Rafuse, H., Sparkes, G., Hinchey, J., & Sandeman, H. (2011). Visible/Infrared spectroscopy (VIRS) as a
597 research tool in economic geology: background and pilot studies from Newfoundland and Labrador. In:
598 *Current Research, Newfoundland and Labrador Department of Natural Resources Geological Survey*
599 *Report 11-1*, 145-166.
- 600 Lane, M. D., Mertzman, S. A., Dyar, M. D., & Bishop, J. L. (2011). Phosphate Minerals Measured in the Visible-
601 Near Infrared and Thermal Infrared: Spectra and XRD Analyses. In: *42nd Lunar and Planetary Science*
602 *Conference Proceedings, The Woodlands, Texas*. p.1013

- 603 Lenz, C., Talla, D., Ruschel, K., Škoda, R., Götze, J., & Nasdala, L. (2013). Factors affecting the Nd³⁺ (REE³⁺)
604 luminescence of minerals. *Mineralogy and Petrology* 107, 415-428.
- 605 Linthout, K. (2007). Tripartite division of the system 2REEPO₄-CaTh (PO₄)₂-2ThSiO₄, discreditation of
606 brabantite, and recognition of cheralite as the name for members dominated by CaTh (PO₄)₂. *The Canadian*
607 *Mineralogist* 45, 503-508.
- 608 Liu, G. (2005). Electronic Energy Level Structure. In: *Spectroscopic Properties of Rare Earths in Optical*
609 *Materials* 83, 1 – 94.
- 610 Mariano, A. N. (1989). Economic geology of rare earth minerals. *Reviews in Mineralogy and Geochemistry* 21,
611 309–338.
- 612 Morin Ka, S. (2012) Hyperspectral characterisation of rare earth minerals. Geological Survey of Western
613 Australia, Record 2012/12, 50 p.
- 614 Mullica, D. F., Milligan, W. O., Grossie, D. A., Beall, G. W., & Boatner, L. A. (1984). Ninefold coordination
615 LaPO₄: Pentagonal interpenetrating tetrahedral polyhedron. *Inorganica chimica acta* 95, 231-236.
- 616 Ni Y., Hughes, J. M., & Mariano, A. N. (1995). Crystal chemistry of the monazite and xenotime structures.
617 *American Mineralogist* 80, 21-26.
- 618 Noe, D. C., Hughes, J. M., Mariano, A. N., Drexler, J. W., & Kato, A. (1993). The crystal structure of monoclinic
619 britholite-(Ce) and britholite-(Y). *Zeitschrift für Kristallographie-Crystalline Materials* 206, 233-246.
- 620 Oberti, R., Ottolini, L., della Ventura, G., & Parodi, G. C (2001). On the symmetry and crystal chemistry of
621 britholite: new structural and microanalytical data, *American Mineralogist* 86, 1066-1075.
- 622 Onac, B. P., Ettinger, K., Kearns, J., & Balasz, I. I. (2005). A modern, guano-related occurrence of foggite, CaAl
623 (PO₄)(OH)₂·H₂O and churchite-(Y), YPO₄·2H₂O in Cioclovina Cave, Romania. *Mineralogy and*
624 *Petrology* 85, 291-302.

- 625 Pasero, M., Kampf, A. R., Ferraris, C., Pekov, I. V., Rakovan, J., & White, T. J. (2010). Nomenclature of the
626 apatite supergroup minerals. *European Journal of Mineralogy* 22, 163-179.
- 627 Pekov, I. V., Pasero, M., Yaskovskaya, A. N., Chukanov, N. V., Pushcharovsky, D. Y., Merlino, S., & Zadov, A.
628 E. (2007). Fluorcalciobriholite, $(\text{Ca,REE})_3[(\text{Si,P})\text{O}_4]_3\text{F}$, a new mineral: description and crystal
629 chemistry. *European Journal of Mineralogy* 1, 95-103.
- 630 Rapaport, A., David, V., Bass, M., Dekka, C., & Boatner, L. A. (1999). Optical spectroscopy of erbium-doped
631 lutetium orthophosphate. *Journal of luminescence* 85, 155-161.
- 632 Roeder, P. L., MacArthur, D., Ma, X. P., Palmer, G. R., & Mariano, A. N. (1987). Cathodoluminescence and
633 microprobe study of rare-earth elements in apatite. *American Mineralogist* 72, 801-811.
- 634 Rowan, L. C., Kingston, M. J., & Crowley, J. K. (1986). Spectral reflectance of carbonatite and related alkalic
635 igneous rocks from four North American localities. *Economic Geology* 81, 857-871.
- 636 Savchyn, P., Karbovnyk, I., Vistovskyy, V., Voloshinovskii, A., Pankratov, V., Guidi, M. C., & Popov, A. I.
637 (2012). Vibrational properties of LaPO_4 nanoparticles in mid-and far-infrared domain. *Journal of Applied*
638 *Physics* 112, 124309.
- 639 Silva, E. N., Ayala, A. P., Guedes, I., Paschoal, C. W. A., Moreira, R. L., Loong, C. K., & Boatner, L. A. (2006).
640 Vibrational spectra of monazite-type rare-earth orthophosphates. *Optical Materials* 29, 224-230.
- 641 Swayze, G.A., Pearson, N., Wilson, S., Benzel, W.M., Clark, R., Hoefen, T.M., Van Gosen, B., Adams, M., &
642 Reitman, J. (2013). Spectrally distinguishing between REE-bearing minerals based on differences in their
643 crystal field $f-f$ transition absorptions. In *Geological Society of America Abstracts with Programs* 45, 278.
- 644 Talla, D., Beran, A., Škoda, R., & Losos, Z. (2011). On the presence of OH defects in the zircon-type phosphate
645 mineral xenotime, $(\text{Y,REE})\text{PO}_4$. *American Mineralogist* 96, 1799-1808.

- 646 Turner, D. J., Rivard, B., & Groat, L. A. (2014). Visible and short-wave infrared reflectance spectroscopy of REE
647 fluorocarbonates. *American Mineralogist* 99, 1335-1346.
- 648 Turner, D. J. (2015). Reflectance spectroscopy and imaging spectroscopy of rare earth element-bearing mineral
649 and rock samples. Unpublished PhD Thesis, University of British Columbia, Canada. 310 pages.
- 650 White, W. B. (1967). Diffuse-Reflectance Spectra of Rare-Earth Oxides. *Applied Spectroscopy*, 21, 167- 171.
- 651 Zhang, M., Salje, E. K., & Ewing, R. C. (2002). Infrared spectra of Si-O overtones, hydrous species, and U ions in
652 metamict zircon: radiation damage and recrystallization. *Journal of Physics: Condensed Matter* 14, 3333.
- 653 Zhang, M., Salje, E. K., & Ewing, R. C. (2003). Oxidation state of uranium in metamict and annealed zircon:
654 near-infrared spectroscopic quantitative analysis. *Journal of Physics: Condensed Matter* 15, 3445.
- 655 Zhang, Y., & Vance, E. R. (2008). Plutonium in monazite and brabantite: Diffuse reflectance spectroscopy
656 study. *Journal of Nuclear Materials* 375, 311-314.

657 **FIGURE CAPTIONS**

- 658 Figure 1. Coordination polyhedra for rare earth element cations in monazite, xenotime, britholite and
659 fluorapatite. Data for polyhedra from Oberti et al. (2001), Ni et al. (1995), and Hughes et al. (1991).
660
- 661 Figure 2. Bond distances for REE polyhedra in monazite, xenotime, britholite and fluorapatite, as
662 described in the text. Multiple bond lengths are indicated where found (e.g., O × 4), the OH bond of
663 REE₂ in britholite and F bond in fluorapatite are labeled, and the vertical bars illustrate the minimum,
664 mean and maximum bond lengths. Data for polyhedra lengths from Oberti et al. (2001), Ni et al. (1995)
665 and Hughes et al. (1991).
666

667 Figure 3. Example of false colour VNIR hyperspectral reflectance imagery (inset, Novo Horizonte “C”),
668 single pixel spectrum (lower spectrum) and average spectrum (upper spectrum). For this particular
669 scene, 2097 pixels were included in a ROI for calculating the averaged spectrum. Crystal measures 0.75
670 × 2.25 cm.

671

672 Figure 4. Chondrite-normalized REE plots for selected samples of monazite (triangles), britholite
673 (squares), and xenotime (×'s).

674

675 Figure 5. Absorption spectra of characterized monazite samples in the VNIR (left, 500 to 1000 nm) and
676 SWIR (right, 950 to 2530 nm) with absorption band clusters shown and the prominent absorption lines
677 of the UofA sample indicated with tick marks. From the top down the spectra are from the Serra Verde,
678 UofA Unk and Elk Mountain samples.

679

680 Figure 6. Spectra of characterized xenotime samples in the VNIR (left, 500 to 1000 nm) and SWIR
681 (right, 950 to 2530 nm) with absorption band clusters shown and the prominent absorption lines of the
682 GQ sample identified with tick marks. From the top down the spectra are from Serra Verde, Gunter
683 Quarry, Novo Horizonte-J and Novo Horizonte-C.

684

685 Figure 7. Spectra of characterized britholite samples in the VNIR (left, 500 to 1000 nm) and SWIR
686 (right, 950 to 2530 nm) with absorption band clusters shown and prominent absorption lines of the
687 CMNOC sample indicated with tick marks. The upper spectrum is from the 001-Mariano sample and the
688 lower is from the CMNOC F90-8 sample.

689

690 Figure 8. Spectrum of fluorapatite in the VNIR (left, 500 to 1000 nm) and SWIR (right, 1000 to 2530
691 nm) with REE-related absorption band clusters shown and prominent absorption lines indicated by tick
692 marks.

693

694 Figure 9. Representative spectra for xenotime (X, top, red), britholite (B, middle, green) and monazite
695 (M, bottom, black) samples in the VNIR range (500 to 1000 nm). Absorption band clusters are shown
696 with bars and prominent absorptions are labeled according to text descriptions.

697

698 Figure 10. Representative spectra for xenotime (X, top, red), britholite (B, middle, green) and monazite
699 (M, bottom, black) samples in the SWIR range (950 to 2530 nm). Absorption band clusters are shown
700 with bars and prominent absorptions are labeled according to text descriptions.

701

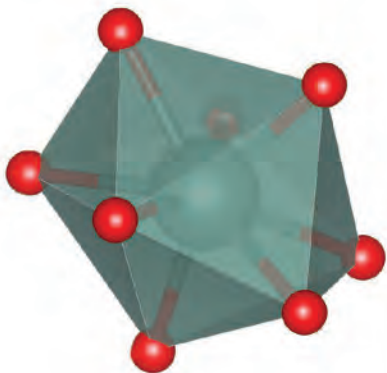
702 Figure 11. Fluorapatite (black, FAP), monazite (blue, MON) and britholite (red, BR) reflectance spectra
703 in the VNIR (left) and SWIR (right, only from 1000 nm to 1800 nm). Note the consistent location of
704 Nd-related absorptions in the VNIR but different morphology and relative intensities, as well as the lack
705 of other REE³⁺ features such as the 978 nm absorption in britholite. Subtle absorptions that are related to
706 bands ascribed to Sm³⁺ and Pr³⁺ in monazite and britholite can also be seen in the SWIR range of the
707 fluorapatite spectrum.

708

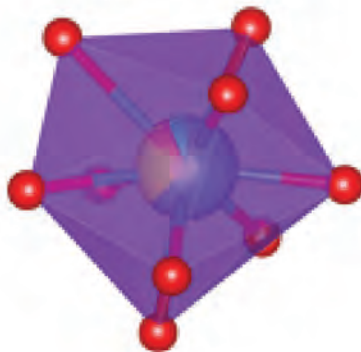
709 Figure 12. Reflectance spectra (left) and continuum-removed spectra (right) near 978 nm for samples
710 showing absorptions at this wavelength. Spectra are labeled and Er and Yb contents are given in
711 parentheses (Er₂O₃ wt.% / Yb₂O₃ wt.%). The continuum-removed plot shows britholite samples with a
712 heavier line weight and “B” labels as well as an “M” label for the single monazite spectrum.

Figure 1

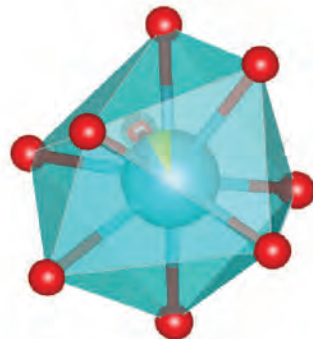
Xenotime
8 coordinated



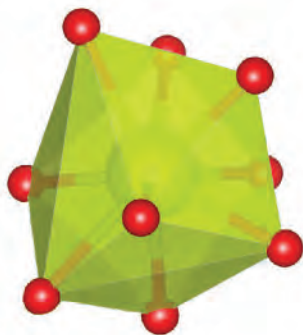
Britholite
REE1 and REE1a sites
9 coordinated



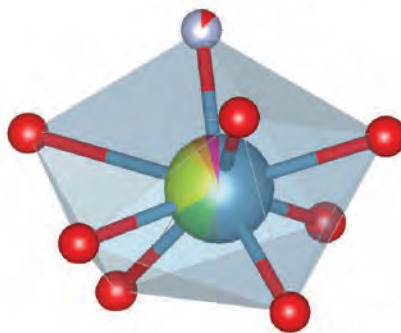
Fluorapatite
Ca1 site
9 coordinated



Monazite
9 coordinated



Britholite
REE2 site
8 coordinated



Fluorapatite
Ca2 site
7 coordinated

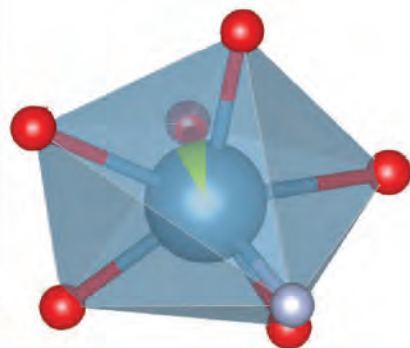


Figure 2

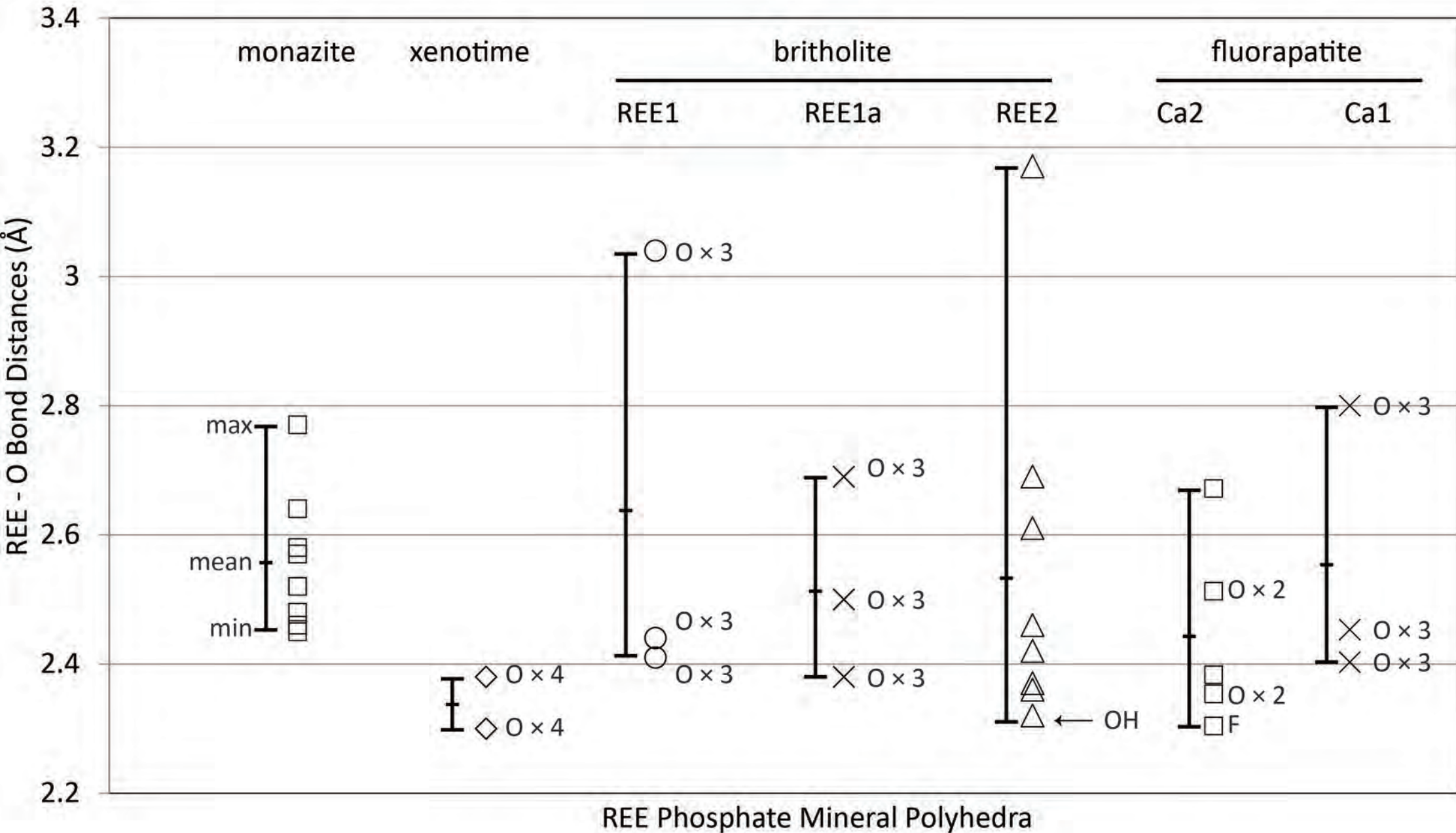


Figure 3

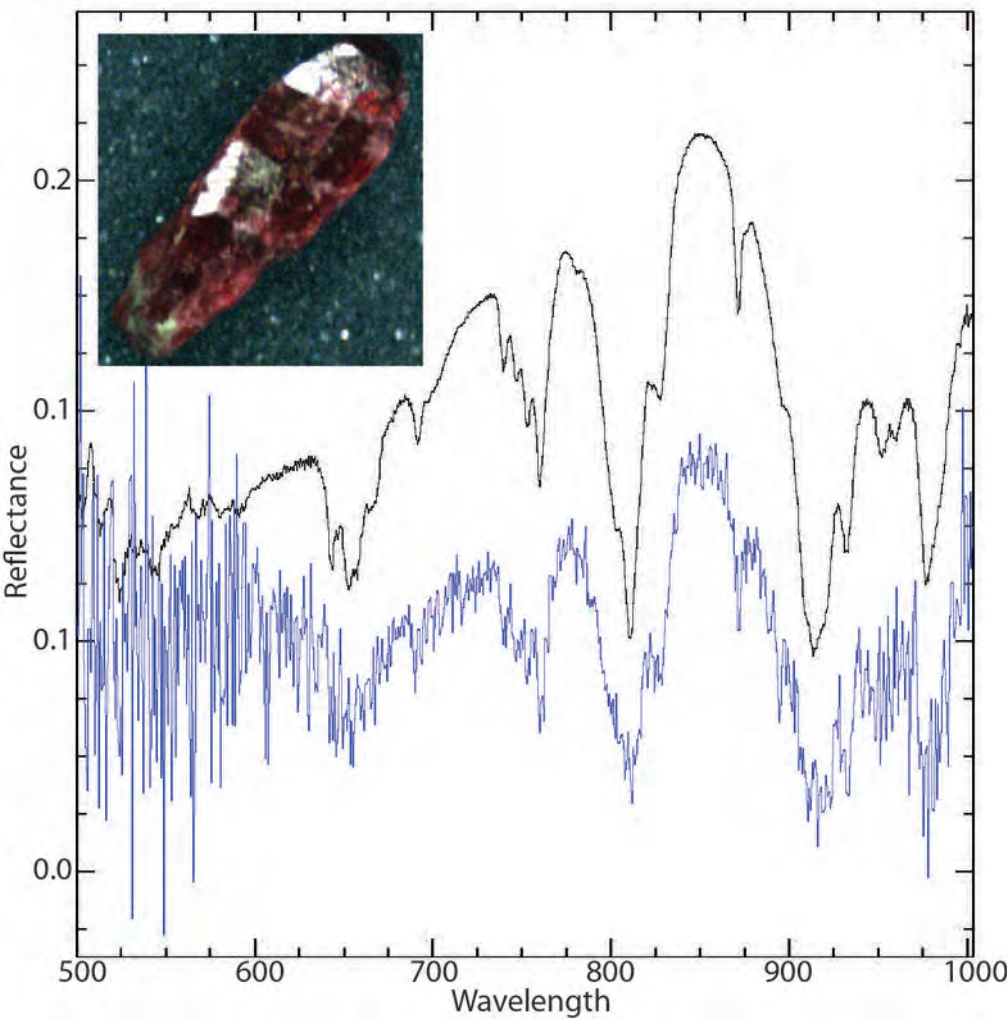


Figure 4

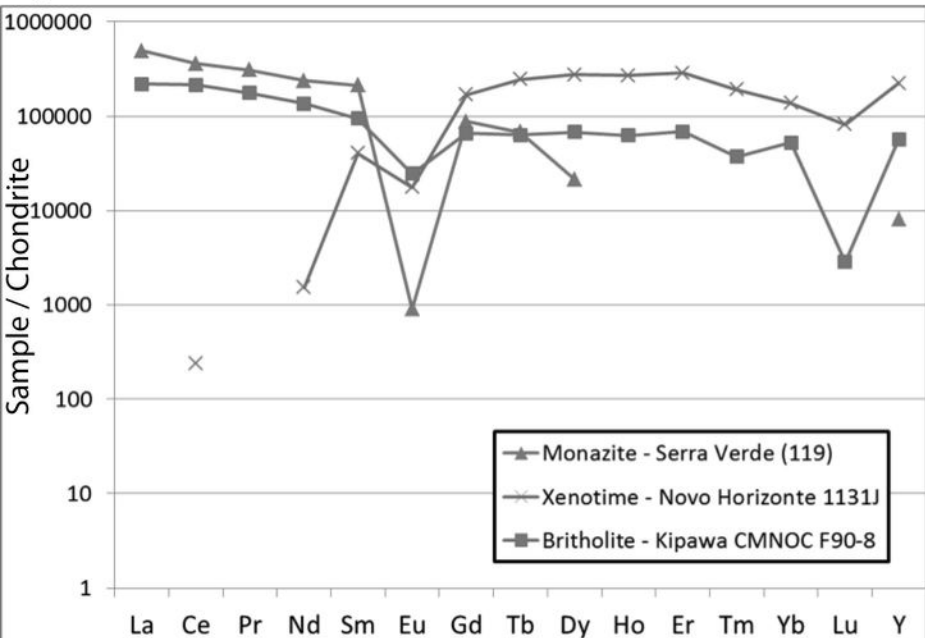


Figure 5

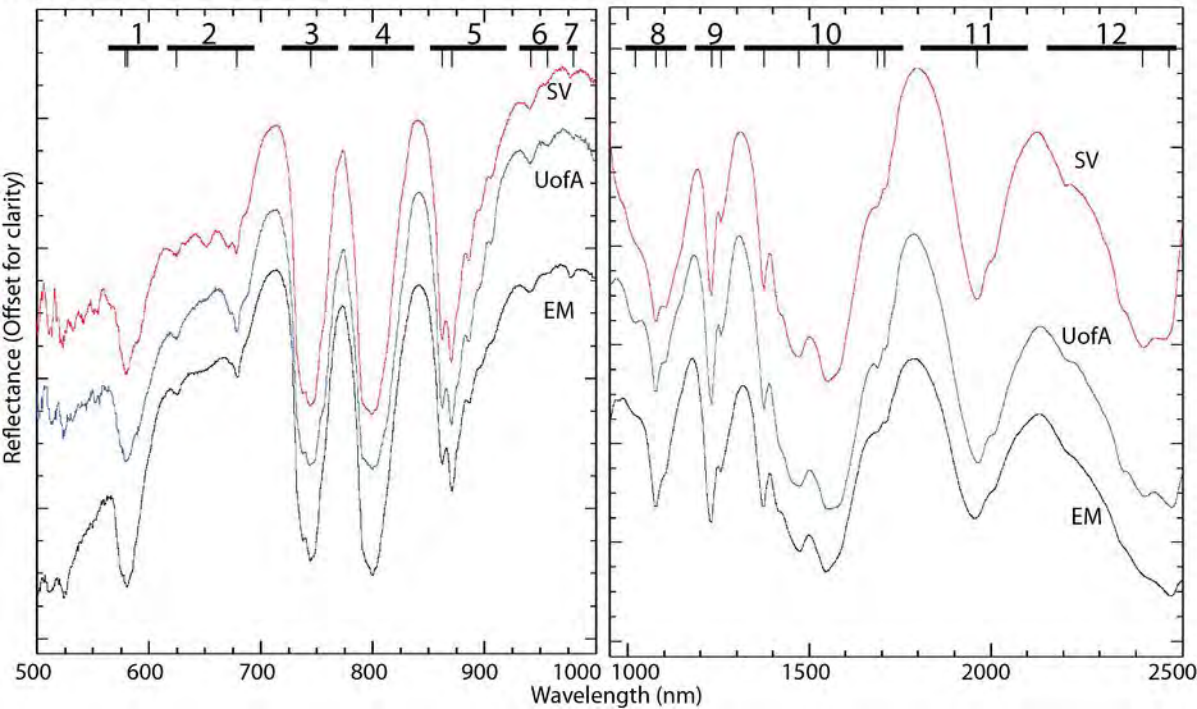


Figure 6

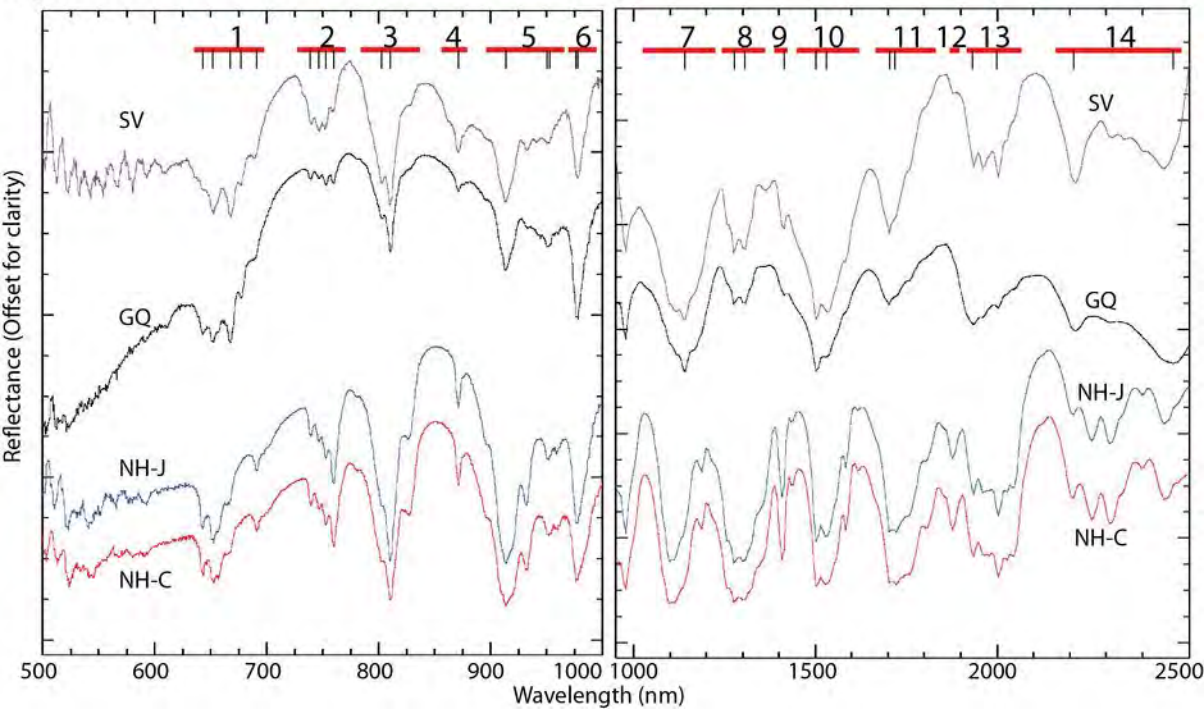


Figure 7

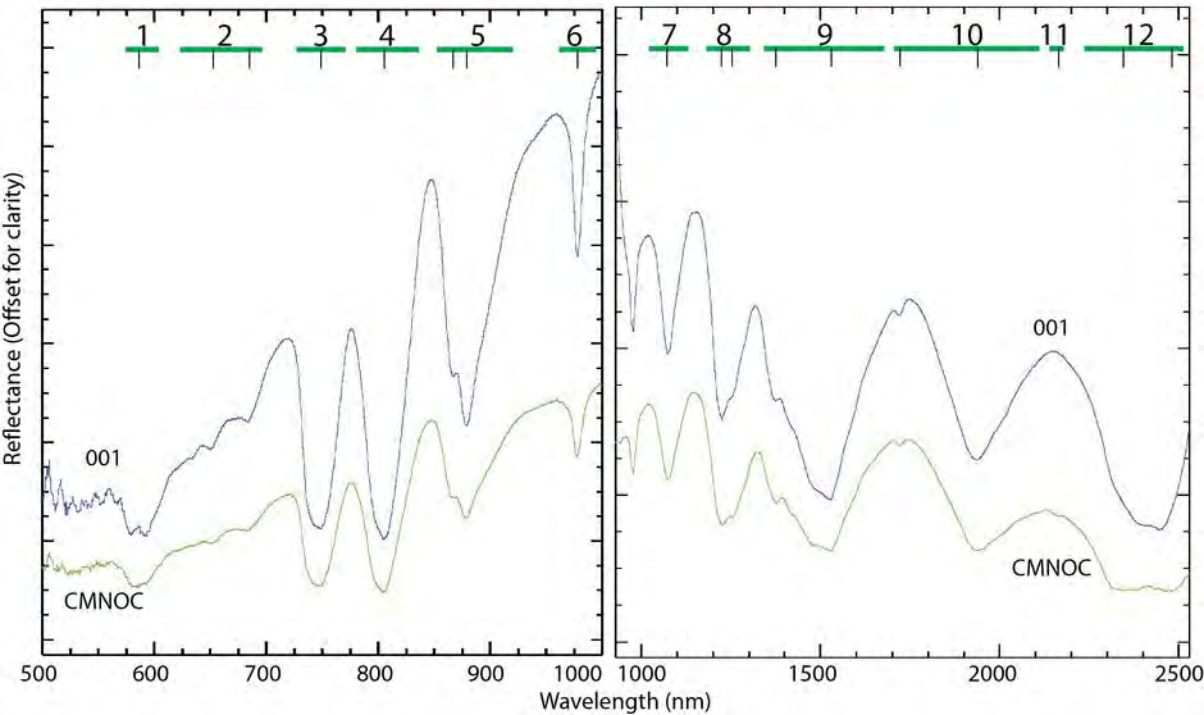


Figure 8

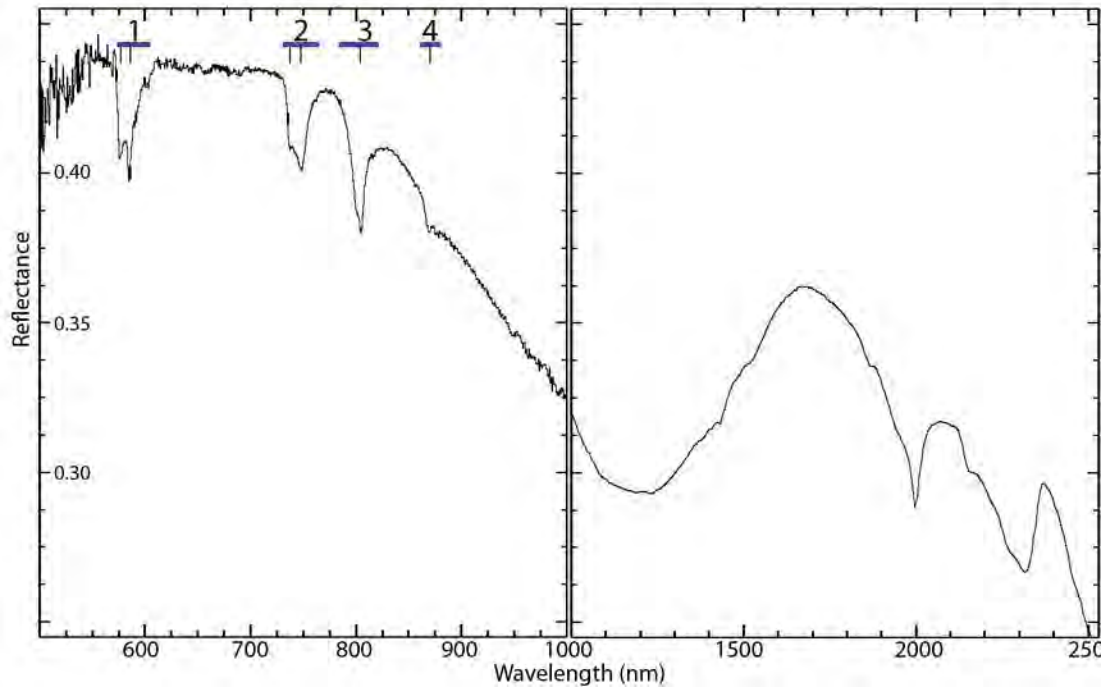


Figure 9

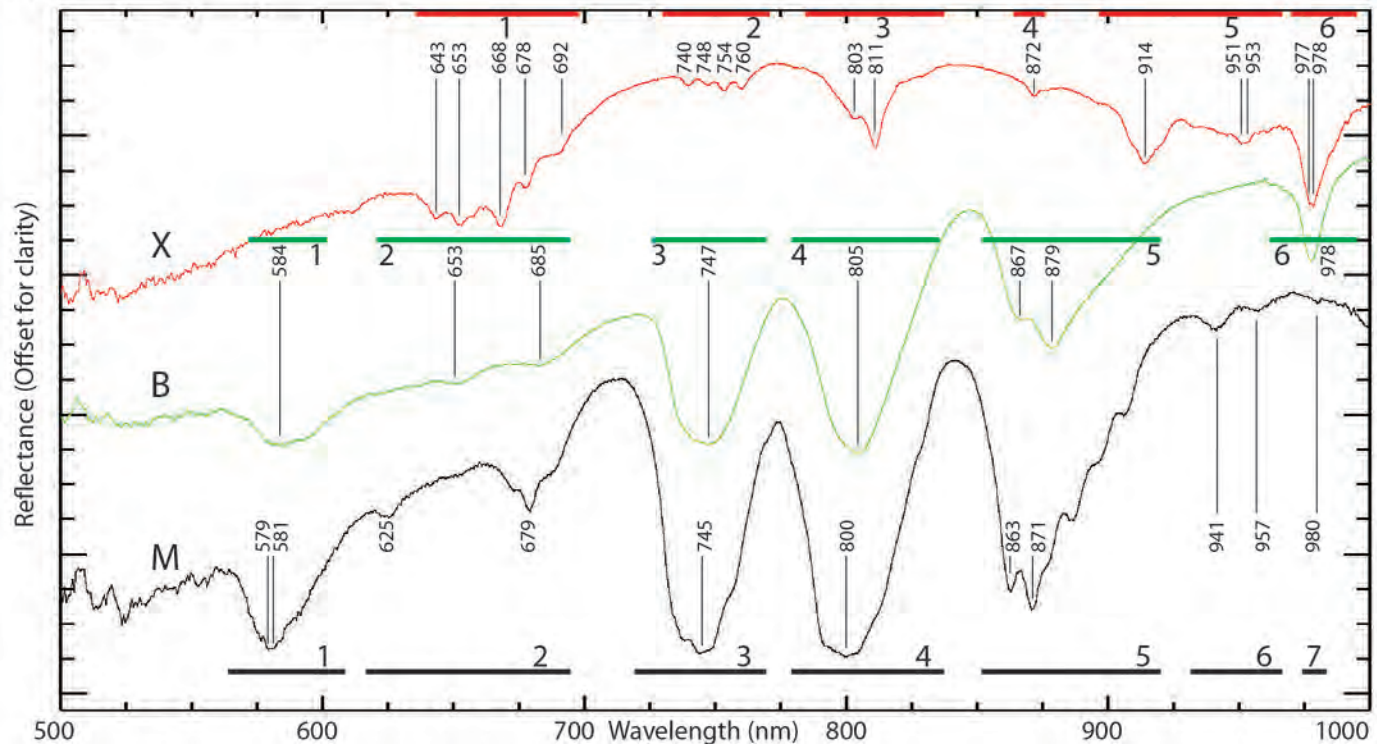


Figure 10

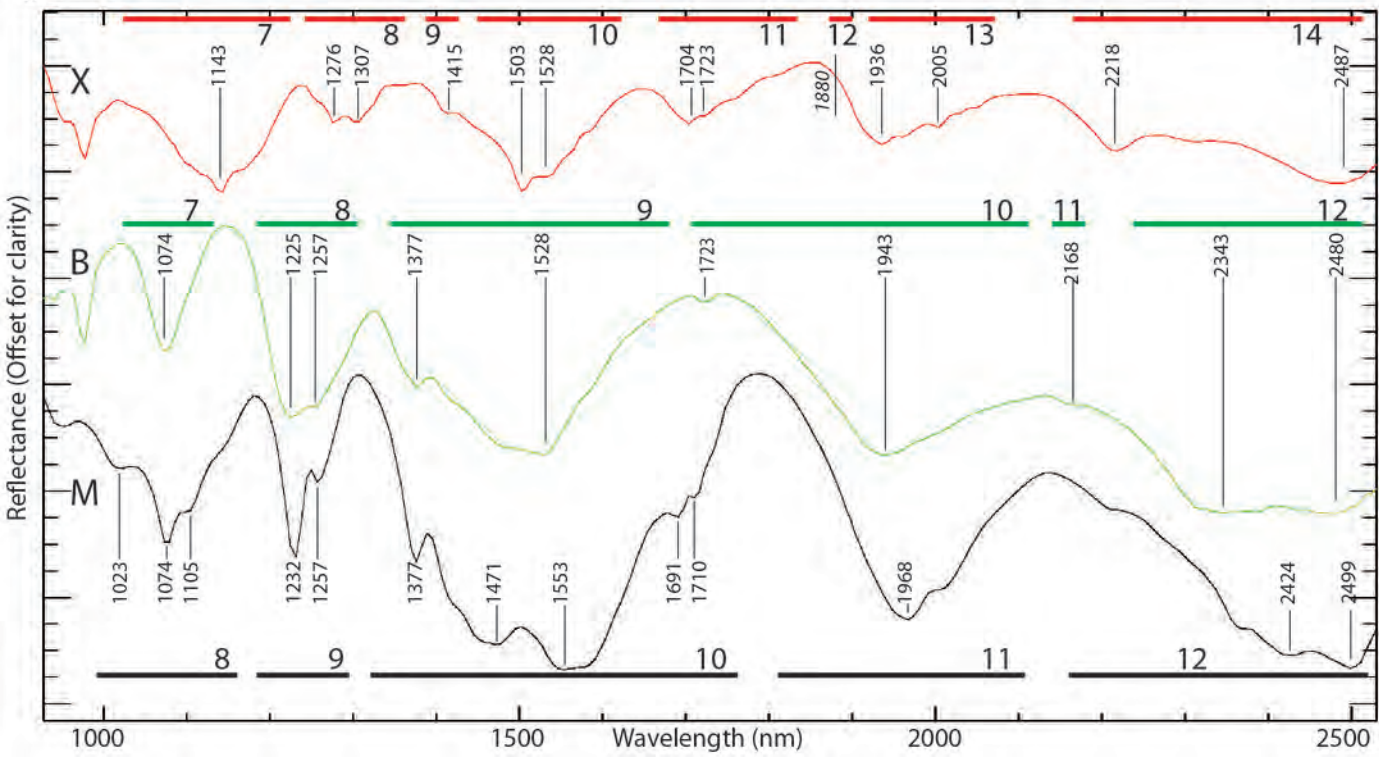


Figure 11

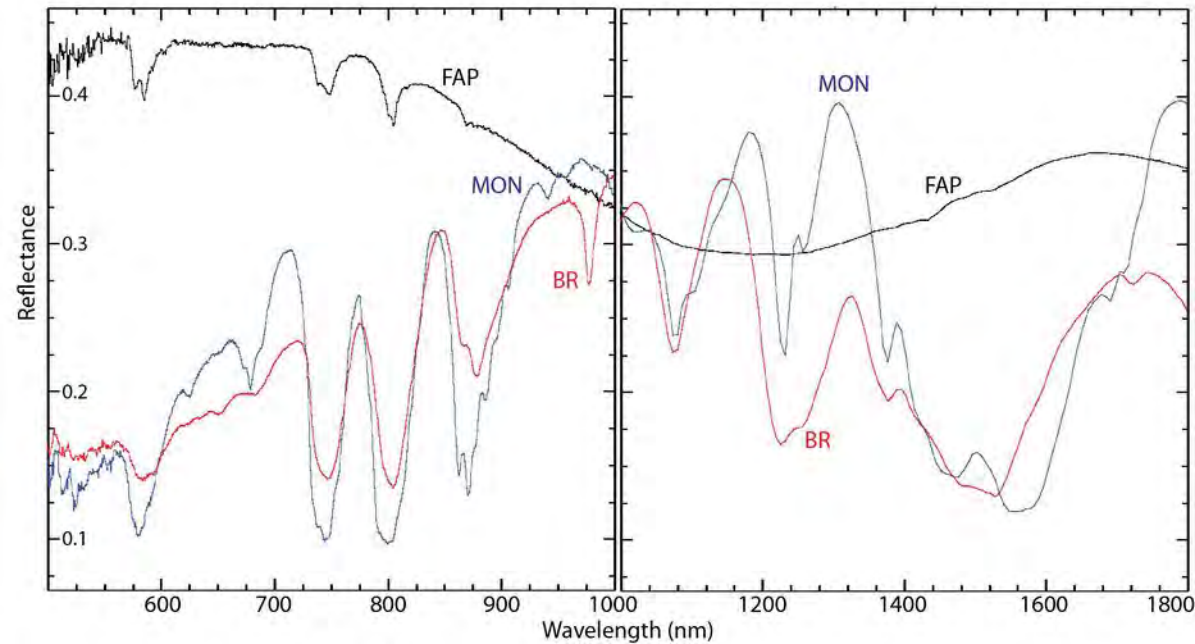


Figure 12

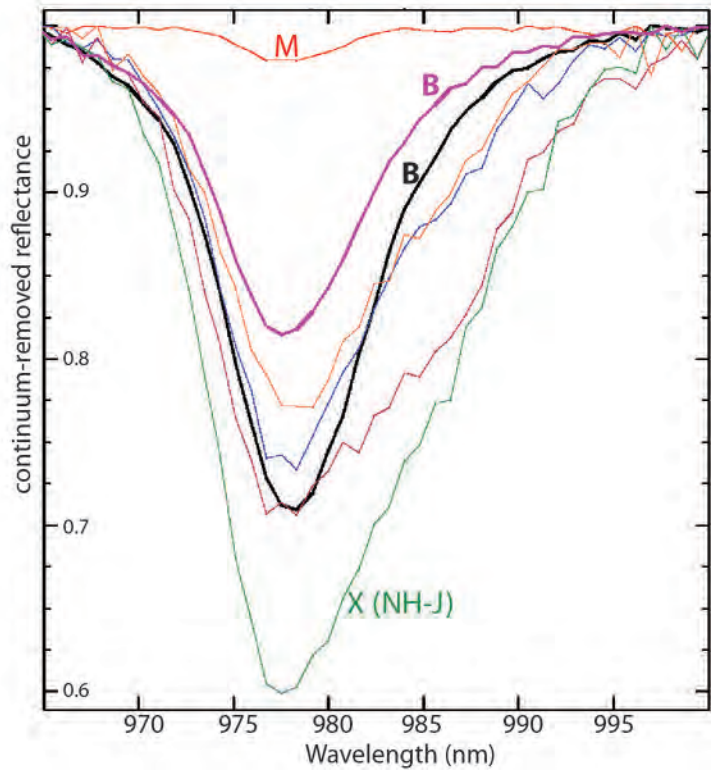
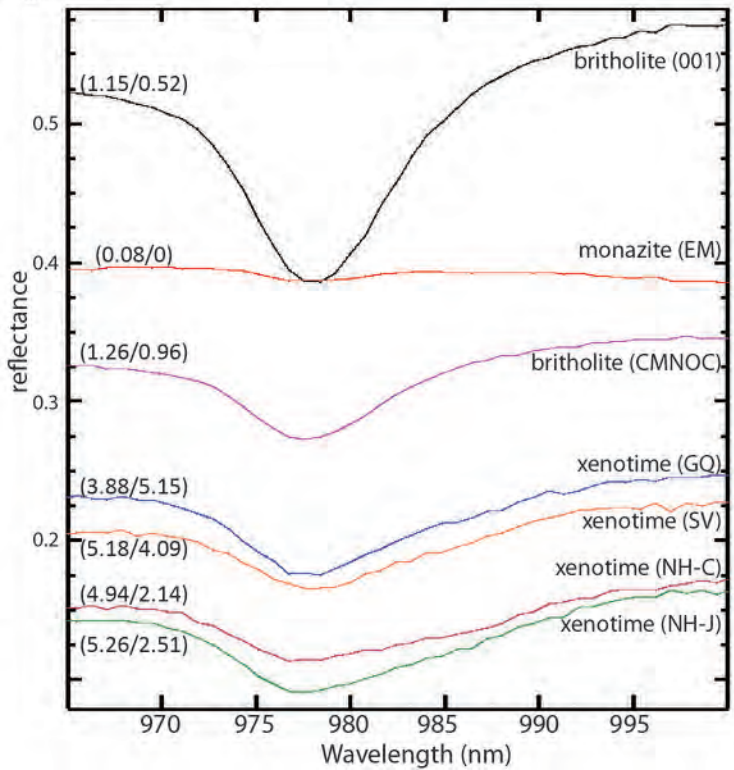


Table 1. Pixel counts per sample used to produce an average spectrum.

Mineral	Sample	VNIR ROI Pixels	SWIR ROI Pixels
monazite	Serra Verde	1995	180
	Elk Mountain	1283	1121
	UofA Unknown	6226	848
xenotime	Serra Verde	1848	215
	Gunter Quarry	2826	419
	Novo Horizonte C	2097	1931
	Novo Horizonte J	5240	4955
britholite	Kipawa CMNOC F90-8	4001	186
	Kipawa Mariano 001	3727	122
fluorapatite	Fir Carbonatite	2898	202

Table 2. Electron microprobe compositions for monazite.

Sample #	119	15-H-7	UofA Unk		119	15-H-7	UofA 537-542 SE
Locality	Serra Verde	Elk Mountain	Unknown		Serra Verde	Elk Mountain	Unknown
# Analyses	5	5	5				
Nb₂O₅				Nb ⁵⁺			
(wt.%)	0.01	0.00	0.09	(apfu)	0.00	0.00	0.00
P₂O₅	25.78	22.62	27.77	P ⁵⁺	0.91	0.85	0.96
SiO₂	1.08	1.90	0.79	Si ⁴⁺	0.05	0.08	0.03
TiO₂	0.01	0.00	0.00	Ti ⁴⁺	0.00	0.00	0.00
ZrO₂	0.04	0.02	0.03	Zr ⁴⁺	0.00	0.00	0.00
UO₂	0.39	0.32	0.05	U ⁴⁺	0.00	0.00	0.00
ThO₂	7.36	12.15	3.55	Th ⁴⁺	0.07	0.12	0.03
La₂O₃	13.56	10.60	14.33	La ³⁺	0.21	0.17	0.22
Ce₂O₃	25.91	22.98	33.16	Ce ³⁺	0.39	0.37	0.49
Pr₂O₃	3.35	3.03	3.84	Pr ³⁺	0.05	0.05	0.06
Nd₂O₃	12.72	11.86	11.42	Nd ³⁺	0.19	0.19	0.17
Sm₂O₃	3.64	4.94	1.90	Sm ³⁺	0.05	0.08	0.03
Eu₂O₃	0.01	0.12	0.02	Eu ³⁺	0.00	0.00	0.00
Gd₂O₃	2.01	2.83	0.42	Gd ³⁺	0.03	0.04	0.01
Tb₂O₃	0.28	0.48	0.00	Tb ³⁺	0.00	0.01	0.00
Dy₂O₃	0.61	1.64	0.08	Dy ³⁺	0.01	0.02	0.00
Ho₂O₃	0.00	0.00	0.00	Ho ³⁺	0.00	0.00	0.00
Er₂O₃	0.00	0.08	0.00	Er ³⁺	0.00	0.00	0.00
Tm₂O₃	0.00	0.00	0.00	Tm ³⁺	0.00	0.00	0.00
Yb₂O₃	0.00	0.00	0.00	Yb ³⁺	0.00	0.00	0.00
Lu₂O₃	0.00	0.00	0.00	Lu ³⁺	0.00	0.00	0.00
Y₂O₃	1.62	0.45	0.11	Y ³⁺	0.04	0.01	0.00
MnO	0.00	0.00	0.02	Mn ²⁺	0.00	0.00	0.00
CaO	0.46	0.64	0.03	Ca ²⁺	0.02	0.03	0.00
Na₂O	0.01	0.02	0.00	Na ⁺	0.00	0.00	0.00
Cl	0.01	0.02	0.03	Cl ⁻	0.00	0.00	0.00
F	0.39	0.36	0.36	F ⁻	0.05	0.05	0.05
O=Cl	0.00	0.00	-0.01	O ²⁻	3.95	3.95	3.95
O=F	-0.16	-0.15	-0.15				
TOTAL	99.08	96.90	97.84	CATSUM	2.01	2.03	1.99
[REE+Y]₂O₃	63.71	59.01	65.28	AN SUM	4.00	4.00	4.00

*Ta, Al, Sr, Mg, Fe, Ba and K were sought but not detected.

*Formula contents on a basis of 4 anions pfu.

Table 3. Electron microprobe compositions for xenotime.

Sample #	1131 C	1131 J	119	CMN F92-15		1131 C	1131 J	119	CMN F92-15
Locality	Novo Horizonte	Novo Horizonte	Serra Verde	Gunter Quarry		Novo Horizonte	Novo Horizonte	Serra Verde	Gunter Quarry
# Analyses	5	5	6	5					
Nb₂O₅ (wt.%)	0.07	0.08	0.06	0.08	Nb ⁵⁺ (apfu)	0.001	0.001	0.001	0.001
P₂O₅	29.12	30.83	32.18	34.16	P ⁵⁺	0.899	0.919	0.938	0.967
SiO₂	0.2	0.23	0.46	0.53	Si ⁴⁺	0.007	0.008	0.016	0.018
TiO₂	0	0.01	0	0	Ti ⁴⁺	0	0	0	0
ZrO₂	0.13	0.11	0.16	0.17	Zr ⁴⁺	0.002	0.002	0.003	0.003
UO₂	0.07	0.01	1.59	0.58	U ⁴⁺	0.001	0	0.012	0.004
ThO₂	0.07	0.33	0.33	0.53	Th ⁴⁺	0.001	0.003	0.003	0.004
Al₂O₃	0	0	0	0.01	Al ³⁺	0	0	0	0
La₂O₃	0	0	0	0	La ³⁺	0	0	0	0
Ce₂O₃	0	0.02	0.04	0	Ce ³⁺	0	0	0.001	0
Pr₂O₃	0	0	0	0.01	Pr ³⁺	0	0	0	0
Nd₂O₃	0.05	0.08	0.29	0.15	Nd ³⁺	0.001	0.001	0.004	0.002
Sm₂O₃	1.05	0.7	0.77	0.34	Sm ³⁺	0.013	0.008	0.009	0.004
Eu₂O₃	0.35	0.12	0	0	Eu ³⁺	0.004	0.001	0	0
Gd₂O₃	5.71	3.88	2.74	1.46	Gd ³⁺	0.069	0.045	0.031	0.016
Tb₂O₃	1.48	1.02	0.87	0.33	Tb ³⁺	0.018	0.012	0.01	0.004
Dy₂O₃	9.75	7.73	6.93	3.58	Dy ³⁺	0.115	0.088	0.077	0.039
Ho₂O₃	1.72	1.67	1.51	1.02	Ho ³⁺	0.02	0.019	0.017	0.011
Er₂O₃	4.94	5.26	5.18	3.88	Er ³⁺	0.057	0.058	0.056	0.041
Tm₂O₃	0.51	0.54	0.66	0.61	Tm ³⁺	0.006	0.006	0.007	0.006
Yb₂O₃	2.14	2.51	4.09	5.15	Yb ³⁺	0.024	0.027	0.043	0.052
Lu₂O₃	0.11	0.23	0.6	0.82	Lu ³⁺	0.001	0.002	0.006	0.008
Y₂O₃	41.82	44.51	42.87	45.72	Y ³⁺	0.812	0.834	0.785	0.813
FeO	0.02	0	0	0	Fe ²⁺	0.001	0	0	0
BaO	0	0	0	0.01	Ba ²⁺	0	0	0	0
CaO	0	0	0.01	0.01	Ca ²⁺	0	0	0	0
Na₂O	0.01	0	0	0	Na ⁺	0.001	0	0	0
Cl	0	0	0	0.02	Cl ⁻	0	0	0	0.001
F	0.3	0.33	0.35	0.51	F ⁻	0.035	0.037	0.038	0.054
O=Cl	0	0	0	0	O ²⁻	3.965	3.963	3.962	3.945
O=F	-0.13	-0.14	-0.15	-0.21					
TOTAL	99.49	100.06	101.54	99.46	CATSUM	2.052	2.036	2.017	1.994
[REE+Y]₂O₃	69.63	68.27	66.55	63.07	AN SUM	4	4	4	4

*Ta, Sr, Mg, Mn, and K were sought but not detected

*Formula contents on a basis of 4 anions pfu.

Table 4. Electron microprobe compositions for britholite.

Sample #	Mariano 001	CMNOC F90-8		Mariano 001	CMNOC F90-8
Locality	Kipawa	Kipawa		Kipawa	Kipawa
# Analyses	5	6			
Nb₂O₅ (wt.%)	0.01	0.02	Nb ⁵⁺ (apfu)	0.001	0.002
P₂O₅	3.03	3.99	P ⁵⁺	0.708	0.854
SiO₂	17.23	20.12	Si ⁴⁺	4.758	5.088
ZrO₂	0.01	0.02	Zr ⁴⁺	0.001	0.002
UO₂	0.22	0	U ⁴⁺	0.014	0
ThO₂	1.26	3.24	Th ⁴⁺	0.079	0.186
La₂O₃	9.01	6.09	La ³⁺	0.918	0.568
Ce₂O₃	17.29	15.4	Ce ³⁺	1.748	1.426
Pr₂O₃	2.04	1.91	Pr ³⁺	0.205	0.176
Nd₂O₃	7.75	7.22	Nd ³⁺	0.764	0.652
Sm₂O₃	1.91	1.63	Sm ³⁺	0.182	0.142
Eu₂O₃	0.07	0.16	Eu ³⁺	0.007	0.014
Gd₂O₃	1.53	1.52	Gd ³⁺	0.14	0.127
Tb₂O₃	0.33	0.26	Tb ³⁺	0.03	0.022
Dy₂O₃	1.93	1.92	Dy ³⁺	0.172	0.156
Ho₂O₃	0.22	0.39	Ho ³⁺	0.019	0.031
Er₂O₃	1.15	1.26	Er ³⁺	0.1	0.1
Tm₂O₃	0.02	0.1	Tm ³⁺	0.002	0.008
Yb₂O₃	0.52	0.96	Yb ³⁺	0.044	0.074
Lu₂O₃	0	0.01	Lu ³⁺	0	0.001
Y₂O₃	9.81	11.35	Y ³⁺	1.442	1.527
SrO	0.03	0.03	Sr ²⁺	0.005	0.004
MnO	0.03	0.02	Mn ²⁺	0.007	0.004
BaO	0	0.01	Ba ²⁺	0	0.001
CaO	16.33	17.57	Ca ²⁺	4.832	4.76
Na₂O	0.08	0	Na ⁺	0.043	0
Cl	0.01	0.05	Cl ⁻	0.005	0.021
F	1.59	1.28	F ⁻	1.389	1.024
H ₂ O *	0.33	0.57	OH ⁻	0.607	0.955
O=Cl	0	-0.01	O ²⁻	24	24
O=F	-0.67	-0.54			
TOTAL	93.07	96.55	Sum [Si]	5.466	5.942
[REE+Y]₂O₃	53.58	50.18	Sum [REE1, 2]	10.755	9.983
			Sum (F, Cl, OH)	2.001	2
			CATSUM	16.219	15.927
			AN SUM	26	26

*Determined by stoichiometry, H₂O calculated assuming 2 (OH⁻, Cl⁻, F⁻) pfu.

**Formula contents on a basis of 26 anions (O+F) pfu.

***Ta, Ti, Al, Mg, Fe and K were sought but not detected.

Table 5. Prominent absorption features of REE-bearing phosphate minerals enriched in LREE in the VNIR range

monazite: UofA_UnkSE				fluorapatite: Fir				britholite: CMNOC												
C#	λ (nm)	shape	Probable Origin	C#	λ (nm)	shape	Probable Origin	C#	λ (nm)	shape	Probable Origin									
1	575	SH	Nd	1	576	MIN - st	Nd	1	584	MIN - b, n	Nd									
	576	MIN - n	Nd																	
	579	MIN - st	Nd																	
	581	MIN - st	Nd																	
	584	MIN - w, n	Nd																	
	592	MIN - w, n	Nd, Pr		602	MIN - w, n	Nd													
2	622	MIN - n	Nd					2	621	SH - n	Nd									
	624	MIN - n	Nd						635	SH - n	Nd									
	625	MIN - n	Nd						653	MIN - n	Er, Ho									
	653	SH - w, n, b	Ho, Er, U?																	
	673	MIN	Nd																	
	676	SH	Nd																	
	679	MIN	Nd						685	MIN - n	Nd									
	689	SH	Nd																	
3	734	SH	Nd	2	738	MIN	Nd	3	743	SH	Nd>Dy									
	738	MIN	Nd									747	MIN - st, b	Nd>Dy						
	745	MIN - st	Nd																	
	747	SH	Nd																	
	749	SH	Nd																	
	757	SH	Nd																	
	770	SH	Nd																	
770	SH	Nd																		
4	792	MIN - w	Nd	3	795	SH	Nd	4	797	SH	Nd>Dy, Er									
	796	MIN - w	Nd									800	MIN	Nd	799	SH	Nd>Dy, Er			
	800	MIN - st	Nd															805	MIN - st, b	Nd>Dy, Er
	804	MIN - w	Nd																	
	814	SH	Nd																	
	830	SH	Nd																	
830	SH	Nd																		
830	SH	Nd																		
5	863	MIN	Nd	4	870	MIN	Nd	5	867	MIN	Nd									
	871	MIN - st	Nd									879	MIN - st	Nd						
	877	SH	Nd																	
	887	MIN	Nd																	
	896	SH	Nd																	
	906	MIN - w	Nd																	
906	MIN - w	Nd																		
6	941	MIN	Sm																	
	957	MIN - w	Sm																	
7	980	MIN - n	Yb>Er					6	978	MIN - st	Yb>Er									

*All lanthanides are considered to be trivalent (Ln^{3+})
C# denotes Cluster Number, as referred to in the text

Table 6. Prominent absorption features of REE-bearing phosphate minerals enriched in LREE in the SWIR range

monazite: UofA_UnkSE				Probable Origin	fluorapatite: Fir				Probable Origin	britholite: CMNOC				Probable Origin			
C#	λ (nm)	shape			C#	λ (nm)	shape			C#	λ (nm)	shape					
8	1023	MIN	Pr						7	1074	MIN - st	Sm					
	1074	MIN - st	Sm							1086	SH	Sm		1105	SH	Sm	
	1105	SH	Sm							1112	SH	Sm					
	1150	SH	Pr														
9	1232	MIN - st	Sm						8	1225	MIN - st	Sm					
	1257	MIN	Sm							1257	SH	Sm > Dy		1288	SH	Dy	
10	1377	MIN	Sm						9	1377	MIN	Sm, Dy					
	1415	SH	H ₂ O							1433	MIN - w	H ₂ O		1415	SH	H ₂ O	
	1452	SH	Pr											1478	SH	Pr	
	1471	MIN	Pr							1522	SH	Sm > Er		1528	MIN - st	Sm > Er	
	1553	MIN	Sm?											1559	SH	Pr	
	1578	SH	Pr											1591	SH	Sm, Pr	
	1691	MIN	Dy, Nd														
	1710	MIN	Nd											10	1723	MIN	Nd, Dy
	1717	SH	Nd														
	1735	SH	Nd														
11	1968	MIN - st	Pr, Sm, H ₂ O							1943	MIN - st	Pr, Sm, H ₂ O					
	2011	SH	Pr, Sm							1986	SH	Pr, Sm		2018	SH	Pr, Sm, Ho	
12	2212	SH	REE/OH/PO ₄							11	2168	MIN	REE/OH/PO ₄				
			REE/OH/PO ₄							12	2318	MIN	REE/OH/PO ₄				
	2368	MIN	REE/OH/PO ₄							2343	MIN	REE/OH/PO ₄					
	2393	SH	REE/OH/PO ₄							2387	MIN	REE/OH/PO ₄					
	2424	MIN	REE/OH/PO ₄							2405	SH	REE/OH/PO ₄					
	2499	MIN	REE/OH/PO ₄							2437	SH	REE/OH/PO ₄					
						2462	MIN	REE/OH/PO ₄									
						2480	MIN	REE/OH/PO ₄									

*Note that dolomite-related absorptions for the fluorapatite spectrum are not listed.

**All lanthanides are considered to be trivalent (Ln^{3+})

C# denotes Cluster Number, as referred to in the text

Table 7. Prominent absorption features of xenotime in the VNIR (left) and SWIR (right) ranges

C#	Novo Horizonte J		Gunter Quarry		Probable Origin	C#	Novo Horizonte J		Gunter Quarry		Probable Origin		
	λ (nm)	shape	λ (nm)	shape			λ (nm)	shape	λ (nm)	shape			
1	643	MIN	643	MIN	Ho>Er	7	1004	SH			Yb, Er		
	647	MIN	648	MIN	Ho, Er				1036	SH	Yb, Er		
	651	MIN	651	MIN	Ho, Er				1080	SH	Sm		
	653	MIN	653	MIN	Ho, Er, U⁴⁺			1099	MIN - st	1099	SH	Dy	
	657	MIN	658	MIN	Ho, Er			1112	MIN	1118	SH	Dy, U ⁵⁺	
	661	SH	661	MIN	Ho, Er			1143	SH	1143	MIN - st	Ho, Dy, U ⁴⁺	
	665	MIN	665	SH	Ho, Er					1168	SH	Dy>Ho	
	667	MIN - n	667	SH	Ho, Er			1187	MIN	1193	SH	Ho, Dy	
	668	SH	668	MIN	Er>Ho		8	1213	SH			Dy, Tm	
	678	SH - n	678	MIN	Er>Ho, Nd			1257	SH	1257	SH	Dy, Sm	
	689	SH	689	MIN - w	Er>Ho, Nd			1276	MIN	1276	MIN	Dy	
	692	MIN	692	SH	Tm > Nd			1301	MIN	1307	MIN	Dy	
	2	740	MIN	740	MIN			Dy>Ho, Nd?	1320	SH	1326	SH	Dy
742		SH	742	SH	Dy>Ho, Nd?	1358		SH	1358	MIN	Dy		
747		MIN	748	MIN	Dy>Ho, Nd?	9		1408	MIN	1415	MIN	H₂O	
753		MIN	754	MIN	Dy>Ho, Nd?		10	1433	MIN	1452	SH	Er	
760		MIN	760	MIN	Dy>Ho, Nd?		1503	MIN	1503	MIN - st	Er>Sm, U⁵⁺		
767		SH - w	767	SH - w	Nd?		1528	MIN	1528	MIN	Er>Sm		
3	781	MIN - w	781	MIN - w	Tm		1559	SH	1559	SH	Er		
	803	MIN	803	MIN	Dy>Er, Nd?		1585	MIN	1585	SH	Er		
	811	MIN - st	811	MIN - st	Dy>Er, Nd?	11	1616	MIN			Dy>Sm, Tm		
	817	SH	817	SH	Dy, Er, Nd?		1660	SH			Dy		
	822	SH	822	MIN	Dy, Er, Nd?		1704	MIN	1704	MIN - st	Dy		
	823	MIN	823	SH	Dy, Er, Nd?		1723	MIN	1723	SH	Dy, Tb		
	826	MIN	826	MIN	Dy, Er, Nd?		1761	SH	1761	SH	Dy, Tb		
	828	SH	829	MIN	Dy, Er, Nd?		1805	MIN	1805	SH	Dy		
	4	872	MIN	872	MIN		Nd	12	1848	SH			Tb, Ho
		876	SH	876	MIN - w		Nd		1880	MIN			Tb, Ho
877		SH	877	MIN - w	Nd		13		1936	MIN	1936	MIN - st	Ho, Tb, H₂O
5	896	SH	896	MIN	Dy, Yb, Ho			1961	MIN	1961	MIN	Ho	
	909	SH	909	SH	Dy, Yb, Ho	1980		MIN	1980	SH	Ho, Sm		
	914	MIN - st	914	MIN - st	Dy, Yb, Ho	2005		MIN - st	2005	MIN	Ho, Sm, Tb		
	920	SH	920	SH	Dy, Yb	2030		MIN	2030	SH	Ho, Sm		
	932	MIN	933	MIN	Dy, Yb	2043		MIN	2049	SH	Ho, Sm		
	951	MIN - n	951	MIN - n	Dy, Yb, Sm	2130		SH			Ho, Sm, Tb		
	953	MIN - n	953	MIN - n	Dy, Yb, Sm	14		2212	MIN - st	2218	MIN	REE/OH/PO₄	
	961	MIN - n	961	MIN - n	Dy, Er, Yb			2262	MIN - st			REE/OH/PO ₄	
	6			977	MIN - st		Yb, Er	2312	MIN - st	2312	MIN	REE/OH/PO ₄	
978		MIN - st	978	MIN - st	Yb, Er		2349	SH			REE/OH/PO ₄		
							2399	MIN			REE/OH/PO ₄		
							2462	MIN	2462	SH	REE/OH/PO ₄		
									2474	SH	REE/OH/PO ₄		
							2499	SH	2487	MIN - st	REE/OH/PO₄		

*All lanthanides are considered to be trivalent (Ln^{3+})
C# denotes Cluster Number, as referred to in the text